Defects in chiral columnar phases: Tilt-grain boundaries and iterated moiré maps

Randall D. Kamien*
School of Natural Sciences, Institute for Advanced Study, Princeton, New Jersey 08540

David R. Nelson
Lyman Laboratory of Physics, Harvard University, Cambridge, Massachusetts 02138
(Received 21 July 1995)

Biomolecules are often very long with a definite chirality. DNA, xanthan, and poly-γ-benzyl-glutamate (PBLG) can all form columnar crystalline phases. The chirality, however, competes with the tendency for crystalline order. For chiral polymers, there are two sorts of chirality: the first describes the usual cholestericlike twist of the local director around a pitch axis, while the second favors the rotation of the local bond-orientational order and leads to a braiding of the polymers along an average direction. In the former case, chirality can be manifested in a tilt-grain boundary phase analogous to the Renn-Lubensky phase of smectic-A liquid crystals. In the latter case, we are led to a new "moiré" state with twisted bond order. In the moiré state, polymers are simultaneously entangled, crystalline, and aligned, on average, in a common direction. In this case the polymer trajectories in the plane perpendicular to their average direction are described by iterated moiré maps of remarkable complexity, reminiscent of dynamical systems.

PACS number(s): 61.30.Jf, 61.43.Hv, 61.72.Bb, 87.15.Da

I. INTRODUCTION AND SUMMARY

It is well known that large molecules play a central role in the structure and function of the cell [1]. In particular, DNA, large polypeptides such as poly-γ-benzyl-glutamate, and polysacharrides such as xanthan are long polymers with a definite and consistent chirality. DNA, with a chain length on the order of centimeters, must be packed into regions with length scales on the order of micrometers, a scale much smaller than the average polymer end to end distance in dilute solution. The packing of these molecules both *in vivo* and *in vitro* is of great interest. In the absence of specialized cellular structures, it is plausible that liquid crystalline phases could facilitate in this packing [2]. It is known that bacterial plasmids can form both nematic and cholesteric liquid crystalline mesophases [3]. In addition, dinoflagellate chromosomes [4] and bacterial nucleoids [5] exhibit cholesteric phases, while sperm heads [6] and bacteriophages [7] exhibit hexagonal columnar phases. Outside the cell, many mesophases arise for long and short chiral biomolecules: columnar phases [8–10], cholesteric phases [9,11,12], nematic phases [13–15], and recently even blue phases [7] have been observed. The possibility of new phases arising in long chiral molecules is intriguing.

In the hexagonal columnar phase of chiral liquid crystals, the crystalline close packing of the molecules competes with the tendency for the molecules to twist macroscopically around each other. As in the twist-grain boundary phase of smectic-A liquid crystals [16], chirality can enter the crystal through the proliferation of screw dislocations. In close analogy with the physics of type-II superconductors, the screw dislocations enter when their energy per unit length is smaller than the energy gain from introducing chirality. When the chiral couplings are small, screw dislocations are excluded and a perfect equilibrium crystalline phase persists, in the same way that the Meissner phase expels an external magnetic field below the lower critical field H_{c1}.

In this paper we elaborate and extend the results presented in [17,18]. As before we neglect structure along the polymer backbones and consider the allowed chiral couplings in the hexagonal columnar phase. We find, in addition to the usual cholestericlike term which favors rotation of the local polymer direction, a new coupling which favors the rotation of the crystalline bond order along the polymer axes. This term leads to a novel phase in which the polymers are braided and in which their trajectories can be described by iterated moiré maps. Modulated chiral phases have been discussed in the context of two-dimensional films [19–21] of chiral tilted molecules. Our new phase is a *three-dimensional* chiral modulated structure. Although the moiré textures we find have some similarity with the blue phases of cholesteric liquid crystals, proposed earlier for chiral polymers [12], they differ in that they *also* incorporate close-packed crystalline order.

We propose two new liquid crystalline phases. The first is the direct analog of the Renn-Lubensky twist-grain boundary phase [16] in which a sequence of polymer crystal regions are separated from each other by tilt-grain boundaries which effect a finite rotation of the aver-

*Present address: Department of Physics and Astronomy, University of Pennsylvania, Philadelphia, PA 19104. Electronic address: kamien@lubensky.physics.upenn.edu

age polymer direction. The director (i.e., the polymer tangent) undergoes a cholestericlike rotation around a pitch axis which is perpendicular to the average polymer direction as well as to the tilt-grain boundaries. We depart here from the notation of Renn and Lubensky in calling these walls "tilt boundaries" rather than "twist boundaries" as in [16]. We use the nomenclature "helical grain boundary" for the honeycomb networks of screw dislocations in the moiré state discussed now. The second set of structures are phases characterized by a sequence of equally spaced parallel helical grain boundaries which cause rotations of the local bond order. These twist-grain boundaries rotate the bond order about an axis parallel to the average polymer direction and perpendicular to the dislocation walls. This new phase leads to complex polymer trajectories which are highly entangled and reminiscent of chaotic dynamical systems. One or more of these phases should appear in sufficiently chiral biopolymers when concentrated in an isotropic solvent. Additionally, we expect that discotic liquid crystals, which also form columnar phases, can exhibit these phases as well if the molecules are chiral. It may also be possible to *induce* the phases we discuss by imposing appropriately twisted boundary conditions on weakly chiral or achiral samples.

In Sec. II we formulate the theory of chiral polymer crystals, introducing the successive degrees of order which separate an isotropic polymer melt from a directed polymer crystal. We show how the sequence of phases progresses through spontaneous symmetry breaking and the nonzero expectations of order parameters. Additionally, we emphasize the analogy of crystals to superconductors [22] and the concomitant analogy of rotational invariance with gauge invariance.

In Sec. III we calculate the line energies of various types of dislocations using continuum elastic theory. We argue that DNA as well as discotic liquid crystals should be in the type-II regime, thus allowing mixed phases with a proliferation of defects.

In Sec. IV we analyze the tilt-grain boundary (TGB) phase of the chiral polymers. Using the continuum elastic theory discussed in Sec. III, we analyze the effect of a wall of screw dislocations on the tilt and twist fields (nematic director and bond order). We estimate the lower critical chiral coupling γ_c for the TGB phase in terms of the Landau parameters. In addition we show in a continuum dislocation density approach that the TGB phase arises naturally as a low energy configuration of screw dislocations. Finally we discuss the x-ray structure function expected for a macroscopic sample.

In Sec. V we analyze the new moiré phase. We calculate the lower critical field γ_c' for this phase to exist as well as the effect on the tilt and twist fields of a single twist wall composed of a honeycomb network of screw dislocations. This phase is also shown, in a continuum "Debye-Hückel" approach, to arise as a low energy configuration of screw dislocations. The braided structure of the moiré phase contains parallel regions of double twist [23] as found in the blue phases of chiral liquid crystals. Unlike the blue phases, however, the order in most cross sections perpendicular to the average polymer direction resembles a perfect triangular lattice.

Finally, in Sec. VI we propose a microscopic structure for the moiré state. We model the polymer trajectories as lines woven by a sequence of moiré maps. We discuss the preferred rotation angles for which moiré patterns appear as well as the scaling statistics of the polymer trajectories. Upon projecting the polymers onto a plane perpendicular to their average directions, we study the scaling of the distance between neighboring paths, leading to Lyapunov exponents. In the Appendix we prove that the special rotation angles that produce moiré maps are irrational fractions of 2π and thus the moiré state is an incommensurate structure: the projected polymer paths never repeat.

II. ROTATIONAL INVARIANCE AND FREE ENERGIES

We first derive the elastic theory of the polymer crystal, starting from phases of higher symmetry. Columnar crystals are solidlike in two directions and liquidlike in one [24]; we assume that the individual monomers in neighboring columns are out of registry, unlike conventional solids which are crystalline in *three* directions. At high temperatures or in the limit of extreme dilution the polymers will be isotropically entangled. We proceed by breaking successive rotational and translational symmetries until a hexagonal columnar phase is reached. All these phases need not exist for a given material; one or more of the intermediate phases could be skipped via a direct first order transition.

A. The polymer nematic phase

When the temperature T is decreased or the density increased, an isotropic polymer melt can transform into a nematic phase [25]. Orientational fluctuations are then described by the usual Frank free energy density:

$$\mathcal{F}_n = \tfrac{1}{2}\{K_1(\nabla\cdot\mathbf{n})^2 + K_2[\mathbf{n}\cdot(\nabla\times\mathbf{n})]^2 + K_3[\mathbf{n}\times(\nabla\times\mathbf{n})]^2\}$$
$$\approx \tfrac{1}{2}[K_1(\vec{\nabla}_\perp\cdot\delta\vec{n})^2 + K_2(\vec{\nabla}_\perp\times\delta\vec{n})^2 + K_3(\partial_z\delta\vec{n})^2] \ , \quad (2.1)$$

where the $\{K_i\}$ are the splay, twist, and bend elastic constants. In the nematic phase we can take $\mathbf{n}\approx\hat{\mathbf{z}}+\delta\vec{n}$ where $\delta\vec{n}$ is a vector in the plane perpendicular to the average director. Here, and in the following, vectors which lie in the plane perpendicular to the average direction of the director will be denoted as $\vec{A}$, while full three-dimensional vectors will be represented by bold face $\mathbf{A}$. We will henceforth take the average nematic direction to be $\hat{\mathbf{z}}$. Because the polymers are long, K_1 is much larger than it would be in a comparable short-chain liquid crystal [26,27], diverging when the polymers becomes infinitely long. In addition, nonlinear effects are known to modify the behavior of K_2 and K_3 and the bulk compression modulus, leading to their anomalous dependence on the polymer lengths [28,29]. If the system were chiral, terms which violate parity transformation would be allowed. In a nematic phase the director has a discrete $\mathbf{n}\rightarrow-\mathbf{n}$ symmetry which must be preserved in the free energy. Since under parity $\nabla\rightarrow-\nabla$, the lowest order chiral term is $\mathbf{n}\cdot(\nabla\times\mathbf{n})$. Note that since every term must

have even powers of $\mathbf{n}$ we can choose to take $\mathbf{n}\rightarrow-\mathbf{n}$ (vector) or $\mathbf{n}\rightarrow\mathbf{n}$ (pseudovector) under parity. For definiteness we take $\mathbf{n}$ to be a vector, though this has no effect on the analysis or results. We write the chiral contribution to the nematic free energy as

$$\mathcal{F}_{\mathbf{n}}^{*}=-\gamma\mathbf{n}\cdot(\nabla\times\mathbf{n})\approx-\gamma\vec{\nabla}_{\perp}\times\delta\vec{n}\ , \tag{2.2}$$

where the two-dimensional pseudoscalar cross product is $\vec{a}\times\vec{b}=\epsilon_{ij}a_i b_j$. One ground state configuration of $\mathcal{F}_{\mathbf{n}}+\mathcal{F}_{\mathbf{n}}^{*}$ is a cholesteric state with pitch $q_0=\gamma/K_2$, although more exotic blue phases are also possible [23]. Nonlinearities associated with rotational invariance are known to modify the relation between γ and q_0 [29].

B. Nematic-hexatic ($N+6$) phase with chirality

At still lower temperatures or higher concentrations a new phase may occur which includes hexatic order in the plane perpendicular to the nematic director $\mathbf{n}$ [30]. Although the present experimental evidence for the hexatic order in polymer nematics is sketchy, such phases seem highly likely in columnar systems, in analogy with the hexatic order possible for vortex lines in high temperature superconductors [31]. There is a complex order parameter ψ_6 which characterizes the local bond order. Its behavior is determined by a Landau theory

$$\mathcal{F}_6=\frac{1}{2}h_1|\mathbf{n}\cdot\nabla\psi_6|^2+\frac{1}{2}h_2|\nabla\psi_6|^2+\frac{r}{2}|\psi_6|^2+\frac{u}{2}|\psi_6|^4\ , \tag{2.3}$$

with $r=a(T-T_6)$. In the ordered phase, for $T<T_6$, $\langle\psi_6\rangle\neq0$ and we may write $\psi_6=|\psi_6|e^{6i\theta_6}$. Sufficiently below the transition we may neglect the fluctuations in the magnitude of the order parameter and employ a Landau theory for θ_6. Upon suppressing an additive constant, $\mathcal{F}_6$ becomes

$$\begin{aligned}\mathcal{F}_6&=\tfrac{1}{2}K_A^{\parallel}(\mathbf{n}\cdot\nabla\theta_6)^2+\tfrac{1}{2}K_A^{\perp}[(\nabla\theta_6)^2-(\mathbf{n}\cdot\nabla\theta_6)^2]\\&\approx\tfrac{1}{2}K_A^{\parallel}(\partial_z\theta_6)^2+\tfrac{1}{2}K_A^{\perp}(\vec{\nabla}_{\perp}\theta_6)^2\ ,\end{aligned} \tag{2.4}$$

where $K_A^{\parallel}=36|\psi_6|^2(h_1+h_2)$ and $K_A^{\perp}=36|\psi_6|^2h_2$ are hexatic stiffnesses parallel and perpendicular to the nematic director and $|\psi_6|^2=a(T_6-T)/4u$. The symmetry $\mathbf{n}\rightarrow-\mathbf{n}$ discussed above for pure nematics must also hold in this phase. However, since θ_6 is measured around $\mathbf{n}$, upon taking $\mathbf{n}\rightarrow-\mathbf{n}$ we must also have $\theta_6\rightarrow-\theta_6$. If, for instance, we had originally measured a change in θ_6 with respect to the right-hand rule using $\mathbf{n}$, we would now see the change go in the opposite direction, with respect to $-\mathbf{n}$. Thus we may have any term quadratic in powers of θ_6 or $\mathbf{n}$. Under parity, θ_6 will change sign if we take $\mathbf{n}$ to transform as a vector, for the same reason it changes sign under nematic inversion. Note that $\theta_6\rightarrow-\theta_6$ is equivalent to $\psi_6\leftrightarrow\psi_6^{*}$. We are now able to write a new chiral term [32] for the "$N+6$" phase. Namely,

$$\mathcal{F}_6^{*}=-i\frac{\Gamma'}{12}\mathbf{n}\cdot(\psi_6^{*}\nabla\psi_6-\psi_6\nabla\psi_6^{*})=-\gamma'\mathbf{n}\cdot\nabla\theta_6\approx-\gamma'\partial_z\theta_6\ , \tag{2.5}$$

where $\gamma'=\Gamma'|\psi_6|^2$. In a nematic ground state with $\mathbf{n}=\hat{\mathbf{z}}$ everywhere (i.e., $\gamma\approx0$), this term will favor a ground state with θ_6 twisting with a pitch $\tilde{q}_0=\gamma'/K_A^{\parallel}$ along the z axis. A similar coupling has been considered before in hexatic smectic-B phases [24] and in cholesteric elastomers [48]. If both γ and γ' are nonzero and q_0 and $\tilde{q}_0$ are incommensurate, one might expect that a chiral $N+6$ polymer melt would resemble an incommensurate smectic [33,32]. These considerations also apply to short-chain nematogens with the same symmetries: if a chiral nematic (or discotic) had the analog of an $N+6$ phase *two* distinct chiral couplings would again be allowed. Table I gives a list of important couplings with their symmetry properties.

There are, in addition to the chiral coupling between $\mathbf{n}$ and θ_6, nonchiral couplings between $\mathbf{n}$ and θ_6 [30,34]. Based on rotational, nematic, and parity invariance, the lowest order terms are

$$\begin{aligned}\mathcal{F}_{\mathbf{n}6}&=\bar{C}(\mathbf{n}\cdot\nabla\theta_6)[\mathbf{n}\cdot(\nabla\times\mathbf{n})]+\bar{C}'\nabla\theta_6\cdot(\nabla\times\mathbf{n})\\&\approx C\partial_z\theta_6\vec{\nabla}_{\perp}\times\delta\vec{n}+C'\vec{\nabla}_{\perp}\theta_6\times\partial_z\delta\vec{n}\ ,\end{aligned} \tag{2.6}$$

where $C=\bar{C}+\bar{C}'$ and $C'=\bar{C}'$. While the final two terms differ only by a total derivative, they are, in principle, different in the presence of topological defects in $\mathbf{n}$ and θ_6.

C. Hexagonal columnar phases with chirality

At still lower temperatures $T<T_{\text{cry}}$ (or high concentrations) the polymers can crystallize in the xy plane. To ensure rotational invariance, and, in analogy with treatments of crystals made up of point particles [35], we build up the crystal out of a superposition of plane density waves with wave vectors $\mathbf{G}_\alpha$. In the case of a triangular lattice we could take, for example, $\mathbf{G}_\alpha=|\mathbf{G}|(\cos(\pi\alpha/3),\ \sin(\pi\alpha/3),0)$ where $\alpha=1,\ldots,6$, $|\mathbf{G}|=4\pi/(\sqrt{3}a_0)$ and a_0 is the lattice constant of the crystal. The $\{\mathbf{G}_\alpha\}$ are the six smallest reciprocal lattice vectors of a triangular lattice and $\mathbf{G}_\alpha\cdot\hat{\mathbf{z}}=0$. The areal polymer density in a plane perpendicular to the average direction may be expanded as

$$\rho\approx\rho_0+\sum_{\alpha=1}^{6}\rho_\alpha(\mathbf{r})\exp\{-i\mathbf{G}_\alpha\cdot\mathbf{r}\}\ , \tag{2.7}$$

TABLE I. Symmetries of a variety of operators. Those with parity ($-$) are chiral. Only combinations which are invariant under nematic symmetry are allowed.

Operator	Symmetry under spatial inversion	Symmetry under nematic inversion
$\mathbf{v}\equiv\nabla\theta_6$	+	−
$\mathbf{n}$	−	−
$\mathbf{v}\cdot\mathbf{n}$	−	+
$\mathbf{v}\cdot(\nabla\times\mathbf{n})$	+	+
$\mathbf{n}\cdot(\mathbf{v}\cdot\nabla)\mathbf{n}$	−	−
$\mathbf{v}\cdot(\mathbf{n}\cdot\nabla)\mathbf{n}$	−	−
$\mathbf{n}\cdot(\mathbf{n}\cdot\nabla)\mathbf{v}$	−	−
$\mathbf{n}\cdot(\nabla\times\mathbf{n})$	−	+
$(\mathbf{v}\cdot\mathbf{n})[\mathbf{n}\cdot(\nabla\times\mathbf{n})]$	+	+

where higher order reciprocal lattice vectors could also be included.

Each plane wave is modulated by a spatially varying magnitude and phase $\rho_\alpha(\mathbf{r})=|\rho_\alpha(\mathbf{r})|\exp\{i\mathbf{G}_\alpha\cdot\vec{u}(\mathbf{r})\}$, where $\vec{u}$ is a two-dimensional displacement field. Under a rotation by $\boldsymbol{\theta}$, the plane waves in (2.7) change. In particular $\mathbf{r}\to\mathbf{r}+\boldsymbol{\theta}\times\mathbf{r}$, and so $\mathbf{G}\cdot\mathbf{r}\to\mathbf{G}\cdot\mathbf{r}+\mathbf{r}\cdot(\mathbf{G}\times\boldsymbol{\theta})$. Thus rotations lead to a position dependent change in $\rho_\alpha(\mathbf{r})$, namely, $\rho_\alpha\to\rho_\alpha\exp\{i\mathbf{G}\cdot(\boldsymbol{\theta}\times\mathbf{r})\}$. Likewise, under a global rotation about the x axis or y axis by an angle θ_x or θ_y, respectively, $\mathbf{n}\to\mathbf{n}+\boldsymbol{\theta}\times\mathbf{n}\approx\hat{\mathbf{z}}+\theta_y\hat{\mathbf{x}}-\theta_x\hat{\mathbf{y}}$, i.e., $\delta\vec{n}\to\delta\vec{n}+\theta_y\hat{\mathbf{x}}-\theta_x\hat{\mathbf{y}}$. Similarly, under a global rotation about the z axis by θ_z, $\theta_6\to\theta_6+\theta_z$. To ensure rotational invariance [22,35], derivatives of $\rho_\alpha(\mathbf{r})$ must be accompanied by the fields θ_6 and $\delta\vec{n}$,

$$\begin{aligned}\mathcal{F}_{\rm cry}=\sum_\alpha\Big\{&\frac{A}{2}|\mathbf{G}_\alpha\cdot[\vec{\nabla}_\perp\rho_\alpha-i\theta_6(\mathbf{G}_\alpha\times\hat{\mathbf{z}})\rho_\alpha]|^2\\&+\frac{B}{2}|\mathbf{G}_\alpha\times[\vec{\nabla}_\perp\rho_\alpha-i\theta_6(\mathbf{G}_\alpha\times\hat{\mathbf{z}})\rho_\alpha]|^2\\&+\frac{C}{2}|\partial_z\rho_\alpha-i(\mathbf{G}_\alpha\cdot\delta\vec{n})\rho_\alpha|^2+\frac{b}{2}|\rho_\alpha|^2\Big\}\\&+c\sum_{\alpha,\beta,\gamma}^{\mathbf{G}_\alpha+\mathbf{G}_\beta+\mathbf{G}_\gamma=0}\rho_\alpha\rho_\beta\rho_\gamma+O(\rho_\alpha^4)\ .\end{aligned}\tag{2.8}$$

Crystalline order arises in this Landau expansion for sufficiently small $b\sim(T-T_{\rm cry})$ so that $\langle\rho_\alpha\rangle\neq0$. Due to the third order term, this transition will, in general, be first order, and $T_{\rm cry}$ represents a limit of metastability. The free energy is the sum of all the terms discussed earlier, namely,

$$F=\int d^3x\{\mathcal{F}_{\rm n}+\mathcal{F}_6+\mathcal{F}_{\rm n6}+\mathcal{F}_{\rm n}^*+\mathcal{F}_6^*+\mathcal{F}_{\rm cry}\}\ .\tag{2.9}$$

The free energy (2.9) is analogous to the Ginzburg-Landau theory of a superconductor. Here, rotational invariance dictates the couplings between Goldstone modes, $\delta\vec{n}$ and θ_6, and derivatives of ρ_α in the same way that gauge invariance dictates the coupling between derivatives of the BCS order parameter ψ and the electromagnetic field $\mathbf{A}$. The contribution $(\mathcal{F}_{\rm n}+\mathcal{F}_6+\mathcal{F}_{\rm n6})$ mimics the field energy $(\nabla\times\mathbf{A})^2$. The two chiral couplings are analogous to the coupling between the magnetic field $\mathbf{B}\equiv\nabla\times\mathbf{A}$ and the external field $\mathbf{H}$ [36]. In our case there are *two* distinct "magnetic fields" $\mathbf{H}$ represented by the chiral couplings γ and γ'.

Upon setting $\rho_\alpha=|\rho|\exp\{i\mathbf{G}_\alpha\cdot\vec{u}\}$ and integrating out $\delta\vec{n}$ and θ_6 we find that these fields become locked to various derivatives of the displacement fields:

$$\begin{aligned}&\delta n_i\approx\partial_z u_i\ ,\\&\theta_6\approx\tfrac{1}{2}\epsilon_{ij}\partial_i u_j\ .\end{aligned}\tag{2.10}$$

The resulting free energy to lowest order in $\vec{u}$ and its derivatives is now

$$F=\int d^3x\left\{\mu u_{ij}^2+\frac{\lambda}{2}u_{ii}^2+K_3(\partial_z^2u_i)^2-\gamma\vec{\nabla}_\perp\times\delta\vec{n}-\gamma'\partial_z\theta_6\right\},\tag{2.11}$$

where $u_{ij}=\frac{1}{2}(\partial_i u_j+\partial_j u_i)$. Here and throughout Roman indices indicate directions only in the xy plane while Greek indices indicate all three coordinate directions. In terms of the parameters in (2.8), $\mu=\frac{3}{4}|\vec{G}|^4|\rho|^2(A+B)$ and $\lambda=\frac{3}{4}|\mathbf{G}|^4|\rho|^2(A-B)$. In contrast with polymer nematics, in the crystal elastic constants do not diverge when the nonlinearities associated with rotational invariance [32] are taken into account. The simplified free energy (2.11) is similar to the Ginzburg-Landau theory in the London limit.

The response of superconductors to an external magnetic field is determined by κ, the ratio of the penetration length to the coherence length. As discussed in the next section, the parameter analogous to κ in hexagonal columnar crystals is typically much greater than 1, showing that these materials behave as type-II rather than type-I superconductors in their response to chirality. In other words, the equilibrium ground states may contain defects.

III. ISOLATED DISLOCATIONS AND THEIR ENERGIES

When dislocations are introduced into the free energy (2.11) $\vec{u}(\mathbf{r})$ is no longer single valued. To account for this, we introduce a new variable $w_{\gamma i}$ which is equal to $\partial_\gamma u_i$ away from the defects [37]. The free energy becomes

$$F=\int d^3x\,\mu\left[\frac{w_{ij}+w_{ji}}{2}\right]+\frac{\lambda}{2}(w_{ii})^2+\frac{K_3}{2}(\partial_z w_{zi})^2-\gamma\epsilon_{ij}\partial_i w_{zj}-\gamma'\partial_z\left[\frac{1}{2}\epsilon_{ij}w_{ij}\right],\tag{3.1}$$

where $\theta_6=\frac{1}{2}\epsilon_{ij}w_{ij}$ and $\delta n_i=w_{zi}$.

Dislocations are restricted so that the Burgers vector $\vec{b}$ must lie in the xy plane and $\mathbf{t}\cdot(\mathbf{n}\times\vec{b})=0$, where $\mathbf{t}$ is the unit tangent point along the dislocation line. The latter constraint eliminates dislocations which add a row of polymer ends [31], which we neglect. We introduce the density tensor $\alpha_{\gamma i}(\mathbf{r})=\int d\mathbf{t}\,d\vec{b}\,t_\gamma b_i\rho(\mathbf{t},\vec{b},\mathbf{r})$, where $\rho(\mathbf{t},\vec{b},\mathbf{r})$ is the volume density of dislocations at the point $\mathbf{r}$ with Burgers vector $\vec{b}$ pointing in the $\mathbf{t}$ direction. Since the dislocations do not end, $\nabla\cdot\mathbf{t}=0$, and $\partial_\gamma\alpha_{\gamma i}\equiv0$. The constraint $0=\mathbf{t}\cdot(\mathbf{n}\times\vec{b})=\mathbf{n}\cdot(\vec{b}\times\mathbf{t})$ becomes, assuming $\mathbf{n}\|\hat{\mathbf{z}}$, $b_x t_y=b_y t_x$, or in the case of many defects $\alpha_{xy}=\alpha_{yx}$. In terms of $w_{\gamma i}$ this constraint reads $\partial_i w_{zi}=\partial_z w_{jj}$, i.e., $\vec{\nabla}_\perp\cdot\delta\vec{n}=-\partial_z w_{jj}\equiv-\partial_z(\delta\rho/\rho)$ ($\delta\rho$ is the fluctuation in the areal density of polymers ρ in a constant-z cross section) which creates the sort of long-range interactions that are central to theories of directed polymers [38,39,27].

Following Ref. [37], we can relate $w_{\gamma i}$ to the density of

dislocations inside a small area Γ as follows:

$$\oint_{\partial\Gamma} ds \frac{du_i}{ds} = -\sum_n b_i^n ,$$

$$\oint_{\partial\Gamma} dx_\gamma \frac{du_i}{dx_\gamma} = -\sum_n \int_\Gamma \mathbf{t}^n \cdot d\mathbf{S}\, b_i^n \delta^2(\mathbf{t}^n \times \mathbf{r}) , \tag{3.2}$$

$$\int_\Gamma dS_\mu \epsilon_{\mu\nu\gamma} \partial_\nu w_{\gamma i} = -\int_\Gamma dS_\mu \alpha_{\mu i} ,$$

where $\partial\Gamma$ is the boundary of Γ and $d\mathbf{S}$ is a directed surface element. It follows that

$$\epsilon_{\mu\nu\gamma} \partial_\nu w_{\gamma i}(\mathbf{r}) = -\alpha_{\mu i}(\mathbf{r}) . \tag{3.3}$$

In Fourier space (3.3) can be solved for $w_{\gamma i}$ and we have

$$w_{\gamma i}(\mathbf{q}) = -i \frac{\epsilon_{\gamma\mu\nu} q_\mu \alpha_{\nu i}(\mathbf{q})}{q^2} + i q_\gamma \psi_i(\mathbf{q}) , \tag{3.4}$$

where it is convenient to decompose the arbitrary function $\psi(\mathbf{q})$ into longitudinal and transverse parts,

$$\psi_i = i \frac{q_i \sigma}{q_\perp^2} - i \frac{\epsilon_{ij} q_j \pi}{q_\perp^2} \tag{3.5}$$

so that $\vec{\nabla}_\perp \cdot \psi(\mathbf{r}) = -\sigma$ and $\vec{\nabla}_\perp \times \psi(\mathbf{r}) = -\pi$. The field $\vec{\psi}$ describes the equilibrium displacement of the polymers in the presence of the dislocation density $\alpha_{\gamma i}(\mathbf{r})$. The extremal equations which result from minimizing (2.11) with respect to variations in $\vec{\psi}$ imply that

$$[(2\mu+\lambda)q_\perp^2 + K_3 q_z^4]\vec{q}_\perp \cdot \vec{\psi} = -\frac{2\mu - K_3 q_z^2}{q^2} \epsilon_{lm} q_z q_l q_j \alpha_{mj} + \frac{\lambda}{q^2} q_\perp^2 \epsilon_{j\mu\nu} q_\mu \alpha_{\nu j} \tag{3.6}$$

and

$$[\mu q_\perp^2 + K_3 q_z^4]\vec{q}_\perp \times \vec{\psi} = -\frac{\mu - K_3 q_z^2}{q^2} q_z q_s q_i \epsilon_{sj} \epsilon_{im} \alpha_{mj} + \frac{\mu}{q^2} q_s q_i q_\rho \epsilon_{sj} \epsilon_{j\rho\nu} \alpha_{\nu i} . \tag{3.7}$$

The three terms on the right-hand sides are sources representing the three different types of dislocation. An edge dislocation lying in the xy plane is a source for the first term in (3.6) while an edge dislocation parallel to the z axis is a source for the second term. The first source contribution in (3.7) is the only nonvanishing term for a straight screw dislocation, while the second is nonvanishing for edge dislocations which lie parallel to the z axis.

Following [40], we can find the effect of dislocations on the nematic twist $\vec{\nabla}_\perp \times \delta\vec{n}$ and bond twist $\partial_z \theta_6$. Let $\omega_\rho = \epsilon_{\rho\alpha j} w_{\alpha j}$. Then, (3.4) leads to $\nabla \cdot \omega = -\mathrm{Tr}[\alpha]$. The definitions $\theta_6 = \frac{1}{2}\epsilon_{ij} w_{ij}$ and $\delta n_i = w_{zi}$ also imply $\nabla \cdot \boldsymbol{\omega} = \partial_y \delta n_x - \partial_x \delta n_y + 2\partial_z \theta_6$. Thus

$$2\partial_z \theta_6 - \vec{\nabla}_\perp \times \delta\vec{n} = -\mathrm{Tr}[\alpha] . \tag{3.8}$$

Since the diagonal components of α_{ij} represent the density of screw dislocations we have related the quantities we are interested in to the macroscopic defect density. Upon referring to (2.10), we see that (3.8) quantifies the noncommutivity of derivatives of $\vec{u}$. By choosing different dislocation complections we can make one or both of $\partial_z \theta_6$ and $\vec{\nabla}_\perp \times \delta\vec{n}$ nonzero and thus take advantage of the chiral couplings in (2.11).

We can now solve for the strain field around a screw dislocation. A screw dislocation in a polymer crystal is shown in Fig. 1, where we have chosen boundary conditions such that $\delta\vec{n} \to \vec{0}$ at $z = \pm\infty$. For a screw dislocation along the x axis, $\alpha_{\gamma i} = \delta_{\gamma x}\delta_{ix}\delta(y)\delta(z)b$ or, in Fourier space, $\alpha_{\gamma i} = 2\pi b \delta_{\gamma x}\delta_{ix}\delta(q_x)$. Immediately from (3.4) we see that $w_{xx} = w_{xy} = 0$. Since $\vec{q}_\perp \cdot \vec{\psi} = 0$ we also have $w_{yy} = w_{zy} = 0$. It follows that

$$w_{yx} = -\frac{2\pi i \delta(q_x) b q_z}{q^2} \left[1 - \frac{q_y^2(\mu - K_3 q_z^2)}{\mu q_\perp^2 + K_3 q_z^4} \right] \tag{3.9}$$

and

$$w_{zx} = \frac{2\pi i \delta(q_x) b q_y}{q^2} \left[1 + \frac{q_z^2(\mu - K_3 q_z^2)}{\mu q_\perp^2 + K_3 q_z^4} \right] . \tag{3.10}$$

From these results we can readily determine the bond twist and nematic twist fields generated by a single screw dislocation with the boundary conditions as above. The bond twist is

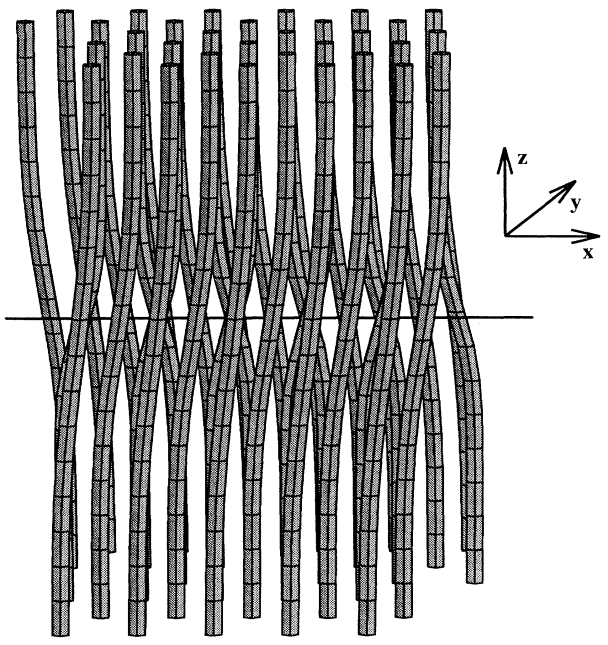

FIG. 1. A single screw dislocation in a polymer crystal. The dark horizontal line is the screw dislocation.

$$\partial_z\theta_6=-\frac{1}{2}\partial_z w_{yx}$$
$$=-\frac{K_3 b}{2}\int\frac{dq_y dq_z}{(2\pi)^2}\frac{q_z^4}{\mu q_y^2+K_3 q_z^4}e^{i(q_y y+q_z z)}$$
$$=-\frac{b}{2}\delta(y)\delta(z)-\frac{b}{16\sqrt{\pi}}\lambda^{-1/2}|y|^{-5/2}e^{-z^2/4\lambda|y|}\times\left\{|y|-\frac{z^2}{2\lambda}\right\}, \quad (3.11)$$

where

$$\lambda=\left[\frac{K_3}{\mu}\right]^{1/2}. \quad (3.12)$$

The nematic twist is

$$\vec{\nabla}_\perp\times\delta\vec{n}=\partial_x w_{zy}-\partial_y w_{zx}$$
$$=\frac{\mu b}{2}\int\frac{dq_y dq_z}{(2\pi)^2}\frac{q_y^2}{\mu q_y^2+K_3 q_z^4}e^{i(q_y y+q_z z)}$$
$$=b\delta(x)\delta(y)+2\partial_z\theta_6 . \quad (3.13)$$

Note that (3.11) and (3.13) are related as in (3.8).

Boundary conditions plays a crucial role in determining the integrated value of the twists. The key issue is whether the boundaries at large $|z|$ go to infinity before or after the boundaries at large $|y|$. It is enlightening to consider, for instance, a vortex disclination in a two-dimensional XY model. While a symmetric configuration with the spins pointing out radially from the core may have the lowest elastic energy, boundary conditions can change this configuration. In an $L\times L$ region of the xy plane we could impose boundary conditions such that the spins are normal to the surfaces at $x=\pm L$. All the winding of the order parameter at the boundaries will occur along the lines at $y=\pm L$. In the case of a dislocation in the columnar crystal, either θ_6 or $\delta\vec{n}$ "wind," depending on the boundary conditions. The boundary condition $\delta\vec{n}\to\vec{0}$ as $z\to\pm\infty$ implies that there is no net twist of the nematic director. In the above example and in Fig. 1 we have enforced this constraint on surfaces at $z=\pm L$ for all values of y. This is equivalent to taking the large y cutoff to infinity first, i.e., $q_y\to 0$. Hence in this case, the integral over a constant x plane of $\partial_z\theta_6$ is

$$\int dy\,dz\,\partial_z\theta_6(\mathbf{r})=\lim_{q_z\to 0}\lim_{q_y\to 0}\partial_z\theta_6(\mathbf{q})=-\frac{b}{2}, \quad (3.14)$$

while the similar integral of $\vec{\nabla}_\perp\times\delta\vec{n}$ is

$$\int dy\,dz\,\vec{\nabla}_\perp\times\delta\vec{n}(\mathbf{r})=\lim_{q_z\to 0}\lim_{q_y\to 0}\vec{\nabla}_\perp\times\delta\vec{n}(\mathbf{q})=\vec{0}. \quad (3.15)$$

The boundary conditions and the order of limits will be of importance when adding up the effects of a collection of defects, as we shall see in the following sections.

Upon inserting the expressions for $w_{\gamma i}$ into (3.1), we find the screw dislocation energy per unit length,

$$f_{\text{screw}}=\frac{1}{L}\int\frac{d^3q}{(2\pi)^3}\left[\frac{\mu}{2}|w_{yx}|^2+\frac{K_3}{2}|q_z w_{zx}|^2\right]$$
$$=\frac{\mu K_3 b^2}{2(2\pi)^2}\int dq_y dq_z\frac{q_z^2}{\mu q_y^2+K_3 q_z^4}$$
$$=\frac{\mu^{3/4}K_3^{1/4}b^2}{2\pi^2\sqrt{\xi_\perp}}\left[\delta\arctan\left[\frac{1}{\delta^2}\right]+\frac{1}{2\sqrt{2}}\ln\left[\frac{\delta^2-\sqrt{2}\delta+1}{\delta^2+\sqrt{2}\delta+1}\right]+\frac{1}{\sqrt{2}}\arctan\left[\frac{\sqrt{2}\delta}{1-\delta^2}\right]\right], \quad (3.16)$$

where

$$\delta=\left[\frac{K_3}{\mu}\frac{\xi_\perp^2}{\xi_z^4}\right]^{1/4}, \quad (3.17)$$

and $\xi_\perp$ and ξ_z are the short-distance y and z cutoffs, respectively. In the two extreme limits, the elastic free energy per unit length becomes

$$f_{\text{screw}}=\begin{cases}\dfrac{\mu^{3/4}K_3^{1/4}b^2}{2\sqrt{2}\pi\sqrt{\xi_\perp}}, & \delta\to\infty\\ \dfrac{\sqrt{\mu K_3}b^2}{4\pi\xi_2}, & \delta\to 0\end{cases} \quad (3.18)$$

so the deciding factor is the dimensionless parameter δ. In analogy with superconductors, δ^2 plays the role of κ, the ratio of the penetration depth to the coherence length. Indeed, suppose for simplicity that the two cutoffs $\xi_\perp$ and ξ_z are comparable ($\xi_\perp\sim\xi_z\equiv\xi$) so that $\delta^2\approx\sqrt{K_3/\mu}/\xi$. From inspection of (2.11), we see that $\lambda=\sqrt{K_3/\mu}$ is the length scale over which bend deformations heal, so $\sqrt{K_3/\mu}$ plays the role of the London penetration depth in a superconducting analogy [24]. Thus δ^2 is the ratio of the healing length of director fluctuations over the healing length of density fluctuations ($\xi\sim a_0$, the lattice constant) which is precisely the form of κ, in superconductors. When $\delta\ll 1$ the polymer crystal is type I and chirality will be excluded until the crystal

breaks down completely, forming a chiral liquid. However, when $\delta \gg 1$ type-II behavior occurs and chirality can creep into the crystal through the proliferation of defects. We must determine the magnitude of δ to decide which sort of behavior we expect.

We first consider chiral polymers, such as DNA. We take $\xi_\perp$ to be the average spacing a_0 between the polymer strands and ξ_z to be on the order of the polymer diameter, or alternatively the base pair spacing in DNA. Then $K_3 = k_B T L_p / \xi_\perp^2$ and $\mu \approx \epsilon_0 / \xi_\perp^2$, where $L_p = \kappa_b / k_B T$ is the persistence length (κ_b is the polymer bending stiffness) and ϵ_0 is the polymer interaction energy per unit length. With the experimental parameters in [41], we have $\xi_z \approx 5$ Å, $\xi_\perp = 30$ Å, $L_p = 550$ Å, and $\epsilon_0 \approx 1.5 k_B T$ Å^{-1} leading to $\delta \approx 5$. Thus we expect type-II behavior.

For dense chiral discotics, we take $\xi_\perp$ and ξ_z to be the respective sizes of the disk-shaped molecules. In this case we expect that $K_3 \sim U_0 / \xi_z$ and $\mu \sim U_0 / (\xi_\perp^2 \xi_z)$ where U_0 is a characteristic interaction energy. If the interactions were entirely steric we would expect that $U_0 \sim k_B T$. Using (3.17) we then find that $\delta = \xi_\perp / \xi_z$. In discotics, as the name implies, $\xi_\perp \gg \xi_z$ and so we expect that they will also be type-II columnar crystals. Note that in the limit of rodlike molecules (as in nematics) $\xi_\perp \ll \xi_z$ and we expect type-I behavior in the hypothetical situation of nematic molecules forming a hexagonal columnar phase.

Straightforward estimates, along the lines taken in [42], show that the screw dislocation core energy per length, when the magnitude of the Burgers vector $b = a_0$ and $\delta \gg 1$, is

$$E_c = c K_3^{1/4} \mu^{3/4} a_0^{3/2} , \tag{3.19}$$

where c is a numerical constant of order unity. Thus E_c is the same order of magnitude as the $\delta \to \infty$ limits of the elastic energy displayed in (3.18).

Considering now an edge dislocation with a Burgers vector of magnitude b and parallel to the z axis $\alpha_{\gamma i} = \delta_{\gamma z} \delta_{ix} b \delta(x) \delta(y)$. The free energy per unit length is [with $\chi = \lambda/(2\mu+\lambda)$]

$$f_{z\ \text{edge}} = b^2 \left\{ \frac{\mu}{256} [128 + 70\chi^2] + \frac{\lambda}{32} [8 - 12\chi + 5\chi^2] \right\} \times \ln \left[\frac{R}{\xi} \right] , \tag{3.20}$$

which, unlike the screw dislocation energy, will diverge as the logarithm of the system size. The core energy is $E_c = c' \mu b^2$ in this case. The logarithmic divergence arises because a vertical edge defect acts on each xy layer as a normal edge dislocation in a two-dimensional crystal.

Unlike infinitely long polymers, discotics can also have edge dislocations lying in the xy plane. For an edge dislocation running along the y axis, we have $\alpha_{\gamma i} = b \delta_{\gamma y} \delta_{ix} \delta(x) \delta(z)$ and find an elastic free energy per unit length

$$f_{xy\ \text{edge}} = \frac{(2\mu+\lambda) K_3 b^2}{2(2\pi)^2} \int dq_x dq_z \frac{q_z^2}{(2\mu+\lambda) q_x^2 + K_3 q_z^4} , \tag{3.21}$$

which is finite, and can be reduced to the complicated expression (3.16) by replacing μ with $(2\mu+\lambda)$ [24].

IV. THE TILT-GRAIN BOUNDARY PHASE

A. Strains, energies, and displacements

The twist-grain boundary state was first proposed as the analog of the Abrikosov flux lattice in chiral smectic-A liquid crystals [16] and later discovered to exist in nature [43]. In analogy with this state, and, as suggested by Kléman [44], the tilt-grain boundary phase of polymers is a crystalline version of a polymer cholesteric, where the cholesteric twist arises from a sequence of low-angle tilt-grain boundaries.

We first consider a single grain boundary. The wall is made up of screw dislocations, pointing along the $\hat{\mathbf{x}}$ direction, stacked up in the xz plane. An example with three screw dislocations is shown in Fig. 2. To determine the twists and strain, we superpose the strains from each individual screw dislocation. With screw dislocations at $z = 0, \pm d, \pm 2d \ldots$, we have

$$[\vec{\nabla}_\perp \times \delta \vec{n}]_{\text{TGB}} = \sum_{n=-\infty}^{\infty} [\vec{\nabla}_\perp \times \delta \vec{n}(x,y,z-nd)]_1 , \tag{4.1}$$

where the notation $[\ ]_1$ refers to the result (3.13) for a single screw dislocation. With the help of the Poisson summation formula (4.1) can be rewritten as a mixed Fourier transform

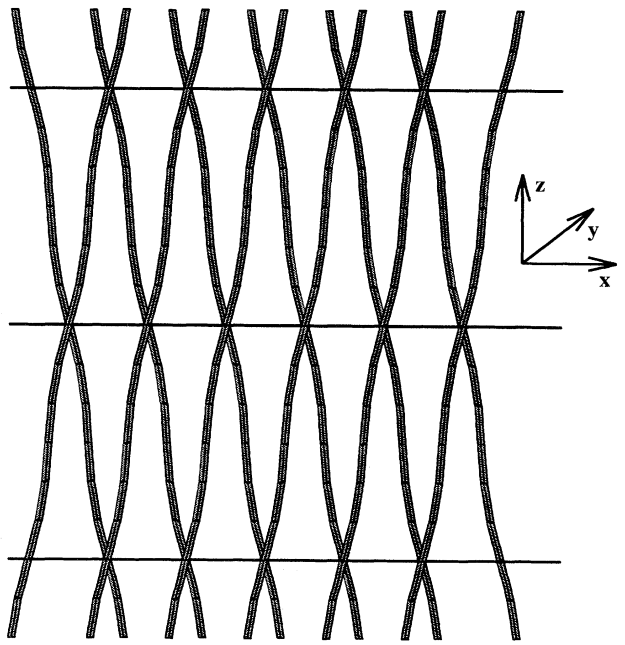

FIG. 2. View of a tilt-grain boundary, looking down the y axis. For clarity we only show the polymer rows immediately behind and in front of the TGB. The heavy lines pointing in the $\hat{\mathbf{x}}$ direction are the screw dislocations.

$$[\vec{\nabla}_\perp \times \delta\vec{n}]_{\rm TGB} = \frac{1}{d}\sum_{m=-\infty}^{\infty} e^{2\pi i m z/d}\left[\vec{\nabla}_\perp \times \delta\vec{n}\left[x,y,q_z=\frac{2\pi m}{d}\right]\right]_1$$
$$= \frac{b}{d}\delta(y)\sum_m e^{2\pi i m z/d} - \frac{(2\pi)^2 b\lambda}{2d^3}\sum_m e^{2\pi i m z/d} m^2 e^{-\lambda(2\pi)^2 m^2 |y|/d^2}, \quad (4.2)$$

where (3.13) has been used in the second line. Since d is small compared to y and z in the far field limit, we approximate the second sum by the first term, the remaining terms being exponentially suppressed:

$$[\vec{\nabla}_\perp \times \delta\vec{n}]_{\rm TGB} \approx b\delta(y)\sum_{n=-\infty}^{\infty}\delta(z-nd) - \frac{(2\pi)^2 b\lambda}{d^3}\cos\left[\frac{2\pi z}{d}\right] e^{-(2\pi)^2\lambda|y|/d^2}$$
$$\approx \frac{b}{d}\delta(y) - \frac{(2\pi)^2 b\lambda}{d^3}\cos\left[\frac{2\pi z}{d}\right] \times e^{-(2\pi)^2\lambda|y|/d^2}. \quad (4.3)$$

Similar manipulations lead to

$$[\partial_z \theta_6]_{\rm TGB} \approx -\frac{(2\pi)^2 b\lambda}{2d^3}\cos\left[\frac{2\pi z}{d}\right] e^{-(2\pi)^2\lambda|y|/d^2}, \quad (4.4)$$

and again (3.8) is satisfied, since now the density of dislocations is precisely $\alpha_{xx} = b\delta(y)\sum_n \delta(z-nd) \approx (b/d)\delta(y)$. In this superposition of many dislocation lines, stacked along the z axis, we implicitly took the limit in which the boundary at large $|z|$ goes to infinity first: It is the $q_z = 0$ term in the Poisson summation formula which puts the Dirac δ function in the expression for $\vec{\nabla}_\perp \times \delta\vec{n}$ and not into $\partial_z \theta_6$.

Upon inserting these results into (2.11), using our earlier results for screw dislocations, and neglecting the interactions between the lines, we find that the threshold chiral coupling above which screw dislocations will penetrate is $\gamma_c = f_{\rm screw}/b$ where $f_{\rm screw}$ includes both elastic and core energies. For $\gamma > \gamma_c$ it becomes energetically favorable for screw dislocations to flood into the crystal and form grain boundaries until their density is limited by the repulsive interactions between screw dislocations. Figure 3 shows a schematic phase diagram for the polymer crystal. The transition to a tilt-grain boundary phase occurs along the γ axis when γ' is small. In the following section we will calculate γ_c', the critical chiral coupling for the bond-order chirality.

The tilt-grain boundary texture is also suggested by a continuum elastic "Debye-Hückel" approach similar to that used in [35] and [31]. This continuum theory requires length scales not only large compared to the lattice constants, but also large compared to the dislocation spacing. We require that the dislocation density $\alpha_{\mu j}$ lead to displacements with finite elastic energies. Suppose there is a configuration which only depends, say, on the y coordinate. In this case it is straightforward to show, using (3.4)–(3.7), that the only configurations with nondivergent elastic energies are those for which $\alpha_{xx}(\mathbf{q}) \to$ const as $\mathbf{q} \to 0$ and all other components of $\alpha_{\mu j}$ vanish in the same limit. We consider only configurations with no edge dislocations parallel to the polymers, as they cost a logarithmically divergent energy per unit length. Upon taking $\alpha_{vj} \propto (2\pi)^2\delta(q_x)\delta(q_z)\delta_{vx}\delta_{jx}$ we see that the only nonvanishing component of $w_{\mu j}$ is $w_{zx} = i\alpha_{xx}/q_y$ which, upon substitution into (3.1) gives $\mathcal{F} = iK_2 q_0 q_y w_{zx}|_{q=0} = -\gamma\alpha_{xx}$. Note that the quadratic contribution to the elastic energy in (3.1) vanishes in this continuum limit. We now add the core energies of the dislocations, leading to the free energy $\mathcal{F}_{\rm DH}$ in the continuum Debye-Hückel approximation:

$$\mathcal{F}_{\rm DH} = E_{ijkl}\overline{\alpha_{ij}}\,\overline{\alpha_{kl}} - \gamma\overline{\alpha_{xx}}, \quad (4.5)$$

where E_{ijkl} is a positive definite matrix of line energies of dislocations lying in the xy plane and $\overline{\alpha_{ij}}$ is the spatially averaged dislocation density tensor. As discussed in [31] the core energies of screw dislocations have the form

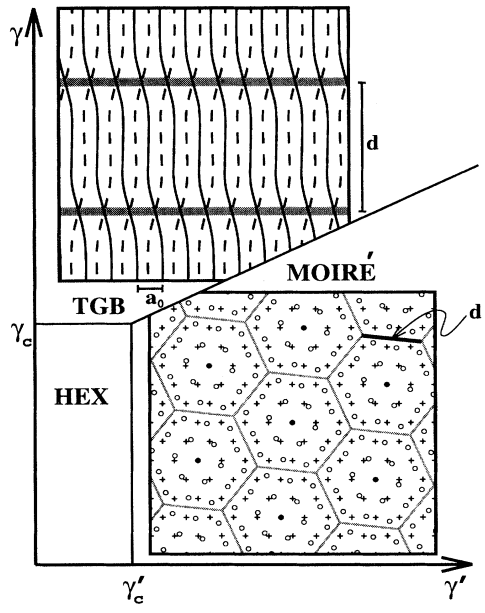

FIG. 3. Phase diagram of a chiral polymer crystal. Insets are representative tilt- (TGB) and moiré-grain boundaries. Shaded lines are screw dislocations. Although we focus here on TGB and helical moiré states, more exotic screw dislocation phases, including those with melted dislocation arrays, could also appear.

$$E_{ijkl}\overline{\alpha_{ij}}\,\overline{\alpha_{kl}}=E_{\text{screw}}(\overline{\alpha_{ii}})^2+E'_{\text{screw}}(\overline{\alpha_{ij}})^2\ , \tag{4.6}$$

where E_{screw} and E'_{screw} are core energies for screw dislocations. In the case of a single dislocation $E'_{\text{screw}}=0$. The minimum of (4.5) occurs when $\overline{\alpha_{xx}}=\gamma/(2E_{\text{screw}}+2E'_{\text{screw}})$, and all other components of α_{ij} vanish. This is precisely the continuum version of the microscopic tilt-grain boundary lattice. In the same approximation, using the relation between w_{zx} and α_{xx}, we find $\delta n_x \equiv w_{zx}=-[\gamma/(2E_{\text{screw}}+2E'_{\text{screw}})]\Theta(y)$, where $\Theta(y)$ is the Heaviside step function, so that across the grain boundary δn_x jumps in proportion to the chiral coupling γ. Since Burgers vectors are quantized in units of the lattice vectors, our proposed periodic array of screw dislocations is the closest allowed approximation to a uniform density.

B. Structure function

A perfect hexagonal close-packed polymer crystal aligned along the z axis will have six primary δ-function Bragg peaks in the q_x-q_y plane at a radius $4\pi/(\sqrt{3}a_0)$, where a_0 is the lattice constant of the polymer crystal.

A tilt-grain boundary, being made of parallel screw dislocations, must also be parallel to an allowed Burgers vector. As a result, if two crystalline regions are joined together by a tilt-grain boundary, they will be rotated with respect to each other around a common reciprocal lattice vector, which we take to be $\mathbf{G}=(4\pi/\sqrt{3}a_0)$ [0,1,0]. Thus, in Fourier space, the six spots will rotate around an axis that passes through one pair of diametric points on the original hexagon. If the illumination volume in a diffraction experiment contains a number of grain boundaries, this rotation will continue, laying out the Bragg peaks along two circles lying in the q_x-q_z plane of radius $2\pi/a_0$ at $q_y=\pm 2\pi/(\sqrt{3}a_0)$. If the angle of rotation is rational there will be discrete Bragg spots around the circle, while if the rotation angle is an irrational fraction of 2π the spots will form a continuous circle. Figure 4 shows a hypothetical structure function for a TGB state with pitch axis parallel to $\hat{y}$ with a rotation angle of $2\pi/7$. A perfectly periodic array of twist-grain boundaries with spacing d' will produce a finely spaced set of additional peaks along the q_y axis centered on $4\pi/\sqrt{3}a_0$ at intervals of $2\pi/d'$ (not shown in Fig. 4). If the tilt-grain boundaries are more irregularly spaced they will nevertheless limit the range of translational correlations along $\hat{\mathbf{y}}$ and all Bragg peaks will be broadened in the q_y direction with a width on the order of $2\pi/d'$, where d' is a translational correlation length.

We expect that due to long-range interactions between the grain boundaries the angles of rotation will lock in at rational fractions of 2π, in analogy with the Renn-Lubensky twist-grain boundary phase [45]. While a detailed calculation of d and d' in terms of the Landau parameters is difficult, we can estimate their sizes by assuming that repulsive interactions between screw dislocations lead to $d\approx d'$. If the Burgers vector has length $b=a_0$, the angle of rotation across each grain boundary is

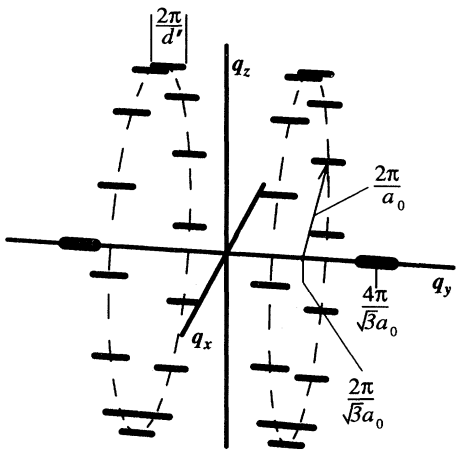

FIG. 4. Structure function of a tilt-grain boundary phase in Fourier space. Due to the interruption of order by grain boundaries spaced along the y axis (with period d'), the Bragg spots are broadened along the q_y axis. This schematic shows a TGB phase with rational rotation angle $\phi=2\pi/7$.

$\phi=\tan^{-1}(a_0/d)$, and thus the pitch is $P=2\pi d'/\phi$. Taking $d\approx d'\gg a_0$ we have $P\approx 2\pi dd'/a_0$. Upon taking a typical cholesteric pitch to be on the order of $P=5000$ Å and the interpolymer spacing to be $a_0=50$ Å, we find that $d\approx d'\approx 200$ Å and $\phi\approx 14°$.

V. THE MOIRÉ PHASE: CONTINUUM ELASTIC THEORY

A. Strains, energies, and displacements

We have seen that a TGB induces a finite jump in the director and only ripples in the bond-orientational order parameter which integrate to zero. We would like to find a dislocation structure which induces a finite jump in θ_6, and thus exploit the chiral coupling γ'.

An attractive possibility is a honeycomb lattice in a constant z plane composed of screw dislocations on its links (see Fig. 3). Such a structure generalizes for three-dimensional systems the grain boundaries discussed in [20]. To calculate the strain fields we must superpose the effect of a collection of finite-length screw dislocations with Burgers vector $\vec{b}$. Consider a collinear row of segments, pointing along $\hat{\mathbf{x}}$, each of length d, separated by $2d$. We can build up a hexagonal lattice by translating, rotating, and superposing the strains or twists from this distribution of defects.

Consider the dislocation density generated by the row discussed above, namely, $\alpha_{\gamma i}=b\delta_{\gamma x}\delta_{ix}\delta(y)\delta(z)\sum_n[\Theta(x-3nd+d/2)-\Theta(x-3nd-d/2)]$. The only nonzero component is, in Fourier space,

$$\alpha_{xx}=\frac{2b\sin(q_x d/2)}{q_x}\sum_m e^{3iq_x md}$$
$$=(4\pi)\frac{b\sin(q_x d/2)}{q_x}\sum_n \delta(3dq_x+2\pi n)\ , \tag{5.1}$$

where we have used the Poisson summation formula. When we Fourier transform back to real space, this becomes

$$\alpha_{xx}(x,y,z)=b\delta(y)\delta(z)\sum_n \frac{\sin(\pi n/3)}{\pi n}e^{i2\pi nx/3d} . \tag{5.2}$$

We neglect the oscillatory contributions, and approximate the sum by the $n=0$ term,

$$\alpha_{xx}\approx\tfrac{1}{3}b\delta(y)\delta(z) . \tag{5.3}$$

Thus the broken line of screw dislocation segments is equivalent at long wavelengths to a solid line with $\frac{1}{3}$ the Burgers vector if we are at distances larger than d. In this approximation, we can replace the honeycomb lattice with a triangular lattice made by extending all the edges to meet at the center of each hexagon, provided we divide the superposition by 3 to restore the correct dislocation density. Proceedings as in the TGB case, we have

$$\begin{aligned}[\vec{\nabla}_\perp\times\delta\vec{n}]_{\text{moiré}}&=-\frac{b}{6\Delta}\left[\frac{\pi}{\lambda\Delta}\right]^{1/2}\sum_m\sqrt{|m|}e^{-\sqrt{\pi m/\lambda\Delta}|z|}\sin\left[\left[\frac{\pi m}{\lambda\Delta}\right]^{1/2}|z|+\frac{\pi}{4}\right]\sum_{j=1}^{3}e^{2\pi im\vec{\eta}_j\cdot\vec{r}_\perp/\Delta}\\&\approx-\frac{b}{3\Delta}\left[\frac{\pi}{\lambda\Delta}\right]^{1/2}e^{-\sqrt{\pi/\lambda\Delta}|z|}\sin\left[\left[\frac{\pi}{\lambda\Delta}\right]^{1/2}|z|+\frac{\pi}{4}\right]\sum_j\cos[2\pi\vec{\eta}_j\cdot\vec{r}_\perp/\Delta] ,\end{aligned} \tag{5.4}$$

with $\vec{\eta}_j=\hat{\mathbf{z}}\times\vec{e}_j$, where $\vec{e}_j$ are the unit lattice vectors of the triangular lattice of polymers and $\Delta=d\sqrt{3}/2$ is the spacing between parallel Bragg planes in that lattice.

Now, $\partial_z\theta_6$ has the δ function:

$$[\partial_z\theta_6]_{\text{moiré}}\approx-\frac{b}{6\Delta}\sum_{j=1}^{3}\delta(z)+\frac{1}{2}[\vec{\nabla}_\perp\times\delta\vec{n}]_{\text{moiré}} . \tag{5.5}$$

To confirm (3.8), note that for a honeycomb lattice, $\alpha_{xx}=\alpha_{yy}=b\delta(z)/(d\sqrt{3})$, so $\mathrm{Tr}[\alpha]=2b\delta(z)/d\sqrt{3}=b\delta(z)/\Delta$.

The honeycomb lattice allows us to exploit the γ' term in (2.11). The integral of $\partial_z\theta_6$ over space from a stack of honeycomb lattices separated by a distance d' along the z axis is $-b/(2\Delta d')$ per unit volume. The total length per unit volume of honeycomb is $2d/d^2\sqrt{3}d'$. Thus, assuming $d,d'\gg a_0$ so that interactions among dislocations are negligible, $\gamma_c'=2f_{\text{screw}}/b$. The region in which we expect the moiré state is shown in Fig. 3. In Fig. 5 we show a set of polymer trajectories and the dislocations leading to them. The moiré state in Fig. 5 contains an inner region of polymers which consist of a single polymer at the center of a bundle of six polymers twisting around it. This texture has double twist in the nematic field as found in the low-chirality limit of blue phases of cholesteric liquid crystals [23,44]. The moiré state takes advantage of both double twist energies and the new chiral coupling γ'. The bond-order field θ_6 and the nematic director $\mathbf{n}$ are linked to each other geometrically—since θ_6 is measured around $\mathbf{n}$, when the director is not uniform we must carefully define θ_6. This leads to the same sort of considerations which occur in He^3-A: the wave function is defined in the plane perpendicular to the nuclear spin axis. The appropriate covariant derivative, which takes the nematic "curvature" into account, is

$$D_\mu\theta_6=\partial_\mu\theta_6-\Omega_\mu , \tag{5.6}$$

where Ω is the connection and its curl is unambiguously given by the Mermin-Ho relation:

$$[\nabla\times\boldsymbol{\Omega}]_\mu=\tfrac{1}{2}\epsilon_{\mu\nu\rho}\epsilon_{\alpha\beta\gamma}n_\alpha\partial_\nu n_\beta\partial_\rho n_\gamma . \tag{5.7}$$

The geometrical connection between the moiré state, the

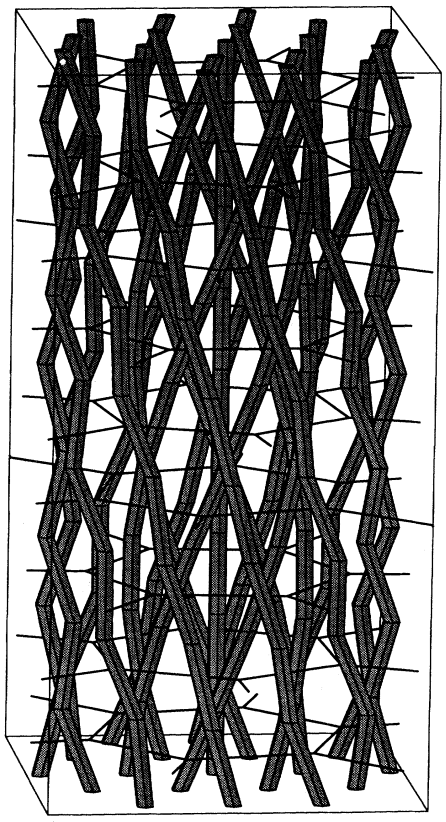

FIG. 5. The moiré state. The thick tubes running in the $\hat{\mathbf{z}}$ direction polymers, while the dark lines are stacked honeycomb arrays of screw dislocations. The intersection of these polymers with any constant z cross section away from the hexagonal defect arrays has the topology of a triangular lattice.

Mermin-Ho relation, and the nearest-neighbor packing of polymers is discussed in [32].

The honeycomb network of screw dislocations described above can also be understood in terms of a continuum approach where one looks for dislocation densities which lead to strains which only depend on the z coordinate. As in the TGB phase we neglect edge dislocations parallel to the polymers and set $\alpha_{zj}=0$. Upon assuming α_{kj} proportional to $(2\pi)^2\delta(q_x)\delta(q_y)$, we find that $w_{zj}=0$ and

$$w_{kj}=\frac{i}{q_z}\begin{bmatrix}\alpha_{yx} & \alpha_{yy}\\ -\alpha_{xx} & -\alpha_{xy}\end{bmatrix}, \quad \begin{matrix}k=x,y\\ j=x,y\end{matrix} . \tag{5.8}$$

Upon substituting this result into (3.1), we find the Fourier transformed free energy

$$\mathcal{F}_{\rm DH}=\frac{\lambda}{2q_z^2}[\alpha_{yx}-\alpha_{xy}]^2 + \frac{\mu}{q_z^2}\left[\alpha_{xy}^2+\alpha_{yx}^2+\frac{1}{2}(\alpha_{yy}-\alpha_{xx})^2\right]+E_{ijkl}\alpha_{ij}\alpha_{kl} - \frac{\gamma'}{2}[\alpha_{yy}+\alpha_{xx}]|_{q=0} . \tag{5.9}$$

In order to eliminate the terms that diverge as $q_z\to 0$, we must take $\alpha_{yx}=\alpha_{xy}$ (i.e., no edge dislocations) and $\alpha_{xy}=\alpha_{yx}=\alpha_{xx}-\alpha_{yy}=0$. Thus $\alpha_{xx}=\alpha_{yy}$ are the only nonzero components of α_{kj}. The minimum of (5.9) occurs at $\overline{\alpha_{xx}}=\overline{\alpha_{yy}}=\gamma'/(8E_{\rm screw}+4E'_{\rm screw})$ where we have used (4.6). Moreover, $\theta_6=\frac{1}{2}(w_{xy}-w_{yx})=-[\gamma'/(8E_{\rm screw}+4E'_{\rm screw})]\Theta(z)$ and so the bond order jumps discontinuously as we go across the helical grain boundary by an amount proportional to the imposed chirality. As in the TGB phase the honeycomb array of screw dislocations is the closest approximation to a uniform sheet distribution of screw dislocations in terms of quantized defects with discrete Burgers vectors.

B. Structure function

The helical grain boundary will rotate the six primary Bragg spots of the structure function of a perfect crystal in Fourier space. In this case all six spots will be swept around a ring in the q_x-q_y plane of radius $|\vec{q}_\perp|=4\pi/(\sqrt{3}a_0)$. If the rotation angle is a rational fraction of 2π there will be a discrete set of spots, while if the angle is an irrational fraction of 2π the spots will form a Bragg ring. While we might expect that interactions between grain boundaries would favor rational lock-in angles, we shall see that the geometry of an isolated helical grain boundary favors an irrational angle. In Fig. 6 we show a schematic structure function for the irrational angle $\phi_3=2\tan^{-1}(\sqrt{3}/21)=9.4°$ obtained by superimposing the structure functions of ten crystalline regions (i.e., nine grain boundaries). An infinite periodic array (spacing d') of twist-grain boundaries would lead to a finely spaced set of Bragg peaks along the q_z axis, at positions $q_z=2\pi n/d'$. If the twist boundaries are spaced more randomly, the translational correlations along $\hat{\mathbf{z}}$ will still be limited to a range of order d'. Reflecting this fact, the

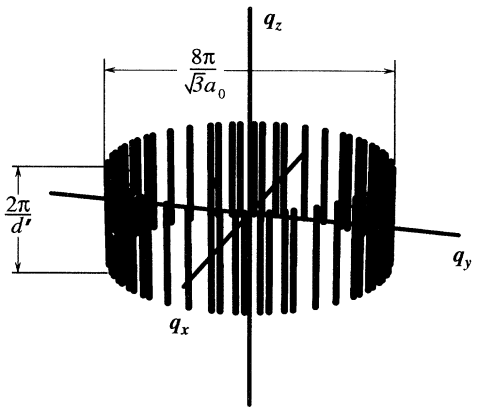

FIG. 6. Structure function of a moiré state in Fourier space. Because of the periodicity along the z axis, the Bragg spots are broadened along q_z. This shows a moiré phase with irrational rotation angle $\phi_3\approx 9.4°$ with ten crystalline regions.

Bragg spots will be broadened along the q_z axis, with a width $\approx 2\pi/d'$, as indicated in Fig. 6. When many incommensurate twist boundaries are included in an illumination volume, the diffraction rods in Fig. 6 will merge into a continuous ring, broad along q_z, but with a very narrow radial width. We have verified this numerically by calculating the scattering from a perfect moiré state composed of 24 grain boundaries. This Fourier transform is axially symmetric about q_z and in Fig. 7 we

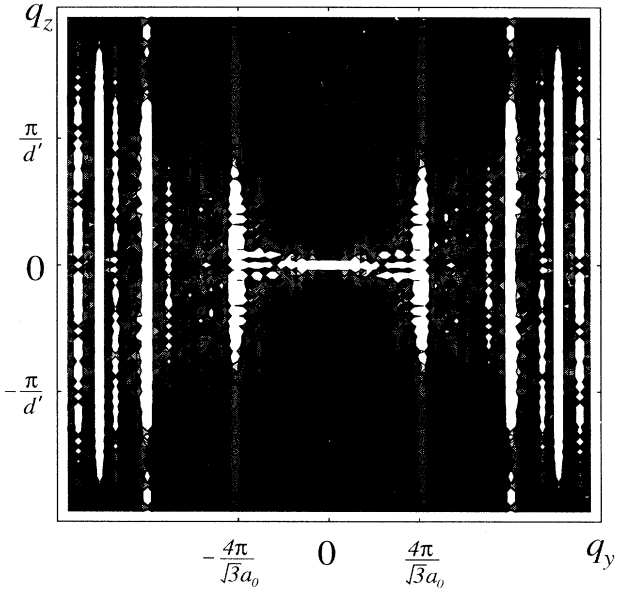

FIG. 7. Numerically computed scattering contours in the q_y-q_z plane for a moiré state with 24 helical grain boundaries. We have scattered from each of 96 beads evenly spaced along each of the 3721 polymers. The structure function is axially symmetric around the q_z axis. This numerical evidence supports the schematic of Fig. 6.

show the structure in the q_y-q_z plane.

From Eq. (5.5) we see that across a helical grain boundary the angle changes by $\phi \approx a_0/2\Delta$ (with $b=a_0$ the minimum Burgers vectors). As in the TGB case, an exact calculation of d and d' would require a detailed accounting of elastic interactions between screw dislocations. We can again estimate their size by taking $d \approx d' \gg a_0$. In this case the pitch is $P=2\pi\sqrt{3}dd'/a_0$. If a typical pitch is $P=5000$ Å and $a_0=50$ Å then we find that $d \approx d'=150$ Å and $\phi \approx 11°$.

VI. THE MOIRÉ PHASE: MICROSCOPIC MODEL

A. Iterated moiré maps

When one rotates one lattice with respect to another around a common point, it is known that at certain angles there will be a nonzero density of points coincident to both lattices [46]. By choosing the rotation angle across the honeycomb dislocation network to produce a high density of coincidence lattice sites [46] we produce especially low strain energies across the boundary. The superposition of triangular polymer lattices below and above the boundary forms a moiré pattern. Figure 8 shows a sequence of four especially simple angles for a triangular lattice. Polymers in the lower half space (circles) must be connected to the closest available polymer in the upper half space (crosses) to minimize bending energy. The map has a discrete translational symmetry, in the sense that any coincidence site could be a center of rotation. Note that an identical moiré pattern could have been obtained by rotating about a point of twofold or threefold symmetry of the coincidence lattice. Especially simple moiré maps arise for the rotation angles

$$\phi_n = 2\tan^{-1}\left[\frac{\sqrt{3}}{3(2n+1)}\right], \tag{6.1}$$

$n=1,2,\ldots$. Figure 8 shows these maps for $n=1,\ldots,4$, with angles $\phi_1 \approx 21.8°$, $\phi_2 \approx 13.2°$, $\phi_3 \approx 9.4°$, and $\phi_4 \approx 7.3°$.

It is shown in the Appendix that all such angles are irrational fractions of 2π [18] so that the structure never repeats upon iteration. Around each coincidence point there are n concentric rings of helical polymers. The lattice of coincidence points is also a triangular lattice, but with a spacing $a_n = a_0\sqrt{1+3(2n+1)^2/2}$, where a_0 is the original lattice constant. The geometrical origin of such energetically preferred lock-in angles has no analog in chiral smectics. The exact choice of lock-in angles and spacing between moiré planes must be settled by detailed energetic calculations. For a *square* lattice an especially simple sequence of lock-in angles is given by

$$\phi_n^{\text{square}} = \tan^{-1}\left[\frac{2n+1}{2n(n+1)}\right], \tag{6.2}$$

leading to coincidence lattice spacings $a_n^{\text{square}} = a_0\sqrt{n^2+(n+1)^2}$ [18].

A schematic of the helical grain boundary energy $E(\phi)$ as a function of angle for $\gamma=\gamma'=0$ is shown in Fig. 9. The deep cusps correspond to the special lock-in angles discussed above. See [47] for a discussion of similar phenomena in conventional crystals. When $\gamma' \neq 0$ the energy has the form

$$\tilde{E}(\phi) = E(\phi) - c\gamma\phi , \tag{6.3}$$

where c is a constant. As γ increases, the preferred minimum eventually jumps from the origin to one of the

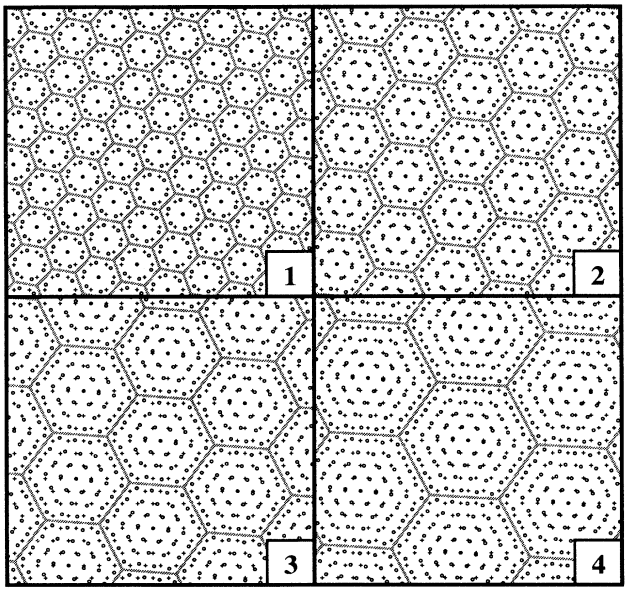

FIG. 8. A single moiré map for triangular lattices with $n=1,2,3,4$ ($\phi_n=21.8°$, 13.2°, 9.4°, 7.3°, respectively). The crosses can be thought of as the ends of polymers in a perfect crystalline region, as can the circles. They join by connecting to the nearest polymer in order to reduce the elastic energy. The shaded lines are the screw dislocations which make up a honeycomb network.

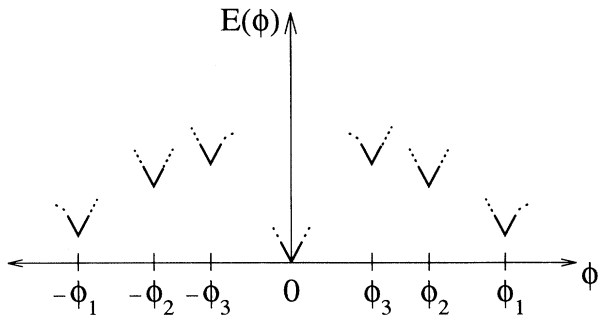

FIG. 9. Change in energy from the ground state of an untwisted crystal as a function of the angle of rotation across a grain boundary, after Balluffi, Komem, and Schober [47]. We expect cusps in the energy around each lock-in angle to grow as $|\phi-\phi_n|$. In a conventional crystal the cusps are sharper, behaving as $|\phi-\phi_n|\ln|\phi-\phi_n|$. Nonetheless, the cusps in the energy landscape will be responsible for the lock in to the special angles ϕ_n.

preferred lock-in angles. In the continuum approach of Sec. IV, we estimated a moiré twist of $\phi \approx 11°$. The $n=3$ moiré state nicely approximates this continuum result with $\phi_3 \approx 9.4°$. In conventional crystals, cusps in the energy landscape near a lock-in angle ϕ_n will have a contribution from the density of extra dislocations, proportional to $\phi-\phi_n$ as well as the logarithmic interaction between the dislocations, leading to the form $\Delta\epsilon \propto |\phi-\phi_n|\ln|\phi-\phi_n|$. In the columnar crystal, due to the softer interaction between dislocations, the leading term in the energy will behave as $\Delta\epsilon \propto |\phi-\phi_n|$ which is still sharp enough to produce the lock-in angles.

It is interesting to consider the effect of the moiré mapping on nearest-neighbor bonds. Consider a polymer crystal at $z=-\infty$. In the xy plane the polymers sit at the sites of a triangular lattice. We may draw lines connecting nearest neighbors as shown in Fig. 10(a), with polymers at the vertices. After allowing various arrangements of screw dislocations to pierce the crystal, we can look again at the polymers in the xy plane at $z=+\infty$. Again, the polymers will sit at the sites of a triangular lattice, typically rotated with respect to the original one. The effect of intervening defects shows up if we undo the rotation but retain the original nearest-neighbor connectivity of the polymers at $z=-\infty$. Figure 10(b) shows the effect of a single screw dislocation, which has "sheared" the polymers on either side with respect to the other. Note that each vertex still has the coordination number 6 it had at $z=-\infty$. As shown in Fig. 11, when moving a bond, in any particular plaquette, we may make one of two types of moves denoted by σ_1 and σ_2. A row of σ_1 or σ_2 moves in a triangular lattice represents the effect of a left- or right-handed screw dislocation, respectively. Note that both moves are area preserving, in that the area of the parallelogram remains unchanged. We may represent the effect of a plane of defects by making a sequence of moves. The restriction of keeping a coordination number of 6 at each vertex amounts to the restriction that dislocation lines may never end and that they must meet in triples at 120°. Figure 10(c) shows the effect of a section of a helical grain boundary, near the intersection of three defect lines.

Upon two iterations of the moiré map separating three regions of polymer crystal, the first coincidence lattice is rotated with respect to the second coincidence lattice by precisely the angle of rotation ϕ_n. Thus the composite coincidence lattice is the "coincidence lattice of coincidence lattices," with lattice constant a_n^2/a_0. Moiré maps iterated p times lead to triangular composite coincidence lattices with spacing $a_n(a_n/a_0)^{p-1}$, i.e., to ever sparser lattices of fixed points with intricate fractal structure in between them. Figure 12 shows the projected polymer paths for a lock-in angle of a square lattice [with $\phi_1=\tan^{-1}(\frac{3}{4})\approx 36.9°$] iterated $p=1,\ldots,4$ times. Note the intricate fractal structure which appears after several iterations of the map.

B. Polymer trajectories and Lyapunov exponents

In contrast to the TGB state polymers braided by moiré maps with $p \gg 1$ are highly entangled and wander far from straight line trajectories. Figure 5 shows the polymer trajectories for the $n=1$ moiré map, of a triangular lattice iterated nine times. In Fig. 13 we show 40 random polymer trajectories after 99 iterations. Although these polymers are clearly influenced by their proximity to a special center of rotation, exceedingly complex trajectories are superimposed on their slow drift around this center. The center becomes less and less noticeable for distant polymers. Using a perfect moiré state with 3721 polymers, we have calculated the average Fourier transform of the monomer density $\rho(q_\perp,q_z)$ of a *single* polymer, averaged over all members of the array. In Fig. 14 we show contour plots of the intensity $\langle|\rho(q_\perp,q_z)|^2\rangle$ in both the q_x-q_y and q_y-q_z plane. Again we see that structure is approximately axially symmetric about q_z. If a dilute concentration of deuterated polymers were introduced into the mix, neutron scattering should produce these incoherent averages. In addition, we have studied numerically the scaling behavior of the polymer size as measured by the components of moment of inertia tensor in the radial and azimuthal directions relative to the

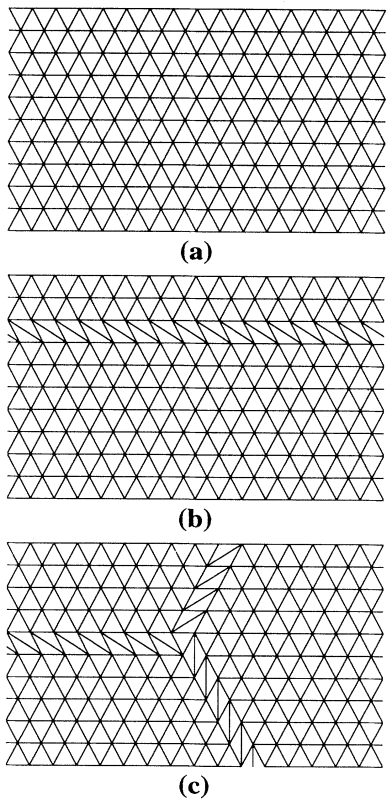

FIG. 10. Connectivity diagram for a polymer crystal. (a) shows the unperturbed connectivity at $z=-\infty$. (b) shows the effect of a single screw dislocation. Note that every vertex has coordination number 6 on the cross section at $z=+\infty$, preserving the nearest-neighbor connectivity of the polymers at $z=-\infty$. (c) shows a section of a honeycomb array of screw dislocations near an intersection of three dislocations. Again the coordination number of every vertex is 6.

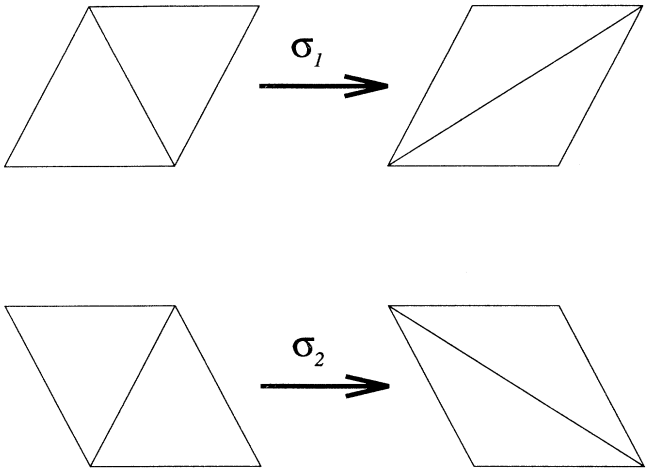

FIG. 11. Allowed moves on a triangular lattice. Note that the moves preserve the area between the four vertices. These moves can be put together to model the effect of dislocation arrays.

center as a function of N, the number of iterations. We expect that the radius of gyration of the projected polymer R should be a function of N and R_0, the radius of the starting point of the polymer trajectory. We postulate for the radial radius of gyration that

$$\frac{R_r(N,R_0)}{R_0}=N^{x_r}A_r\left[\frac{N^{y_r}}{R_0}\right]. \tag{6.4}$$

For large R_0 or small N, we find that the radial R_r and

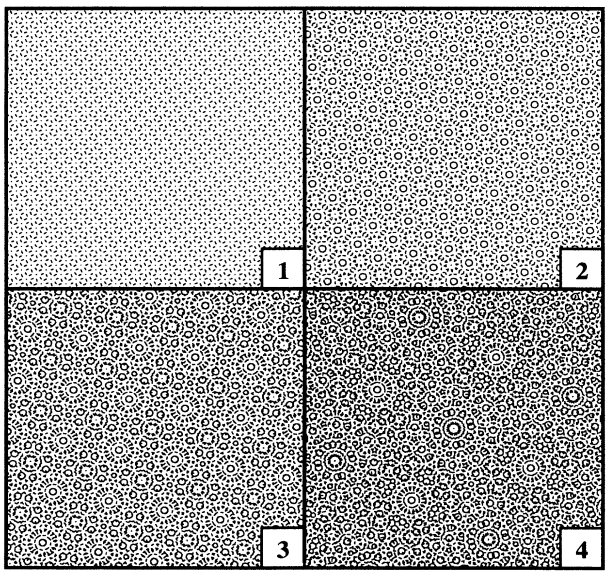

FIG. 12. The projected top view of a moiré map on a square lattice with rotation angle $\tan^{-1}(\frac{3}{4})$. The four boxes show the projected polymer paths after $p=1,2,3,4$ iterations.

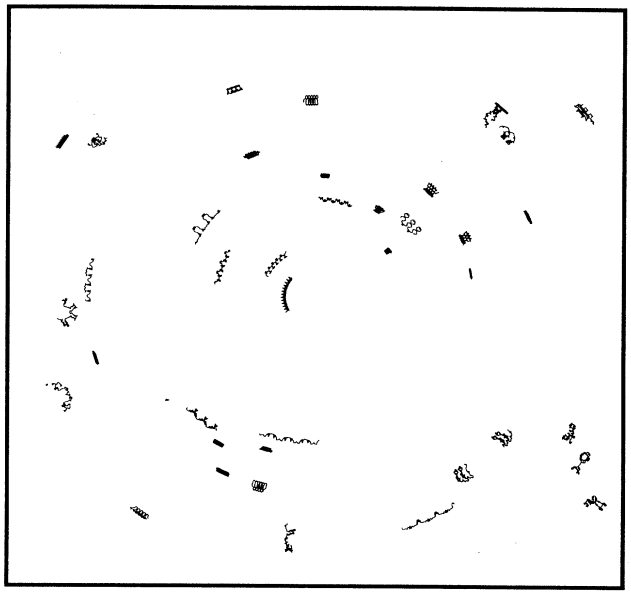

FIG. 13. A projected top view of 40 random polymer paths resulting from the moiré map with $n=1$ iterated 99 times. There is an exceptional fixed point of all 99 maps at the center.

azimuthal R_ϕ radii of gyration do not depend on R_0 and both scale as $N^{1/2}$, i.e., as a simple random walk in the xy plane. Thus as $z\to 0$, $A_r(z)\sim z$ and $x_r+y_r=\frac{1}{2}$. Similarly, the azimuthal radius of gyration scales as

$$\frac{R_\phi(N,R_0)}{R_0}=N^{x_\phi}A_\phi\left[\frac{N^{y_\phi}}{R_0}\right], \tag{6.5}$$

and again we find that $x_\phi+y_\phi=\frac{1}{2}$ and $A_\phi(z)\sim z$ as $z\to 0$. These observations suggest the one parameter scaling form

$$\frac{R_i^2(N,R_0)}{R_0^{\eta_i}}=\mathcal{F}_i\left[\frac{N}{R_0^{\eta_i}}\right], \tag{6.6}$$

where $\eta_i=1/y_i$, $i=r$, ϕ, and the scaling functions $\mathcal{F}_i(z)\sim z$ as $z\to 0$. Figure 15 suggests that, superimposed on the small N "random walk" behavior is a slow drift around the rotation center in the azimuthal direction. This drift represents the effect of the distant exceptional coincidence site. As the polymers spread around the circle at radius R_0 they appear to stay confined to an annular region of width $\sim R_0$. For simplicity we take $\eta=\eta_r=\eta_\phi$. We choose η so that the points of crossover to ballistic (for R_ϕ) and constant (for R_r) behavior collapse. We find $\eta=1$ gives the best collapse. In Fig. 15 we show the radius of gyration data for 1364 polymer trajectories around a supercoincidence site of 99 $n=1$ moiré maps. We have binned the data into 30 equal width annuli and assigned an average R_0 to each bin. The figure clearly shows that $x_i+y_i=\frac{1}{2}$. After the crossover points $R_r(N,R_0)\to$const and $R_\phi(N<R_0)\sim N$, as expected. In the radial case, there is a second crossover point in

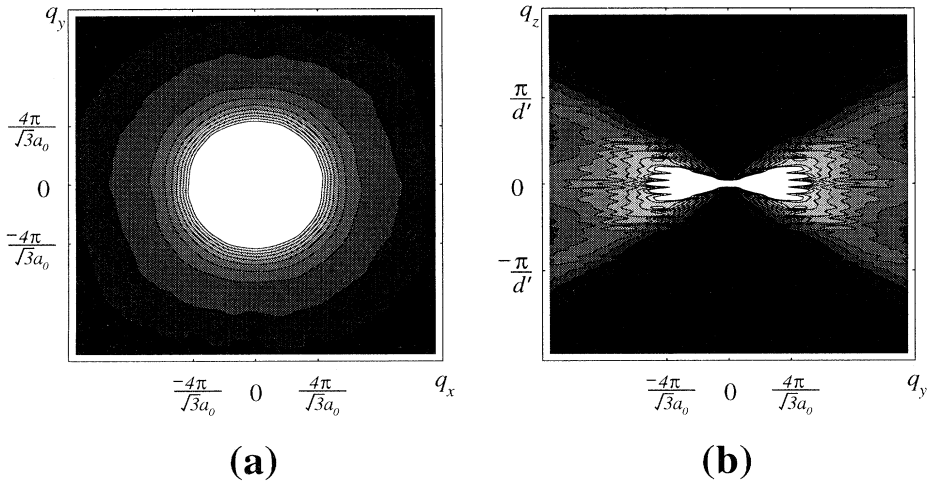

FIG. 14. Numerically calculated average Fourier transform of the monomer density of a single polymer in the (a) q_x-q_y and (b) q_y-q_z planes. We expect that a dilute concentration of deuterated polymers would produce neutron scattering profiles similar to these. The plots were made from the same data set as in Fig. 7.

$R_r(N,R_0)$, presumably where the polymers have made a complete circle around the supercoincidence site. This second crossover is evident in the plot only for small values of R_0.

Not only do the polymers spread from their starting point, but they also diverge from their neighbors. Figure 16 shows seven polymers which start as nearest neighbors. After 99 iterations they separate from each other, as shown by their trajectories Consider a pseudodynamics under which the z axis becomes time and we consider the trajectories of the polymers as the trajectories of two-dimensional particles. We can look at the average square distance between pairs of neighboring polymers and consider the scaling of the separation as a function of N, in the spirit of measuring a Lyapunov exponent in a real dynamical system. We have performed this numerical experiment with the same set of 1364 polymers used to study the radius of gyration. We calculate $\Delta=\sqrt{\langle|\delta\vec{r}_i-\delta\vec{r}_j|^2\rangle}\equiv\sqrt{\Delta_r^2+\Delta_\phi^2}$, where $\delta\vec{r}_i$ is the displacement of polymer i from its starting point, and where the average is over all i and j which are nearest neighbors. Again, we postulate scaling forms for the root mean square radial and azimuthal separations $\Delta_r(N,R_0)$ and $\Delta_\phi(N,R_0)$:

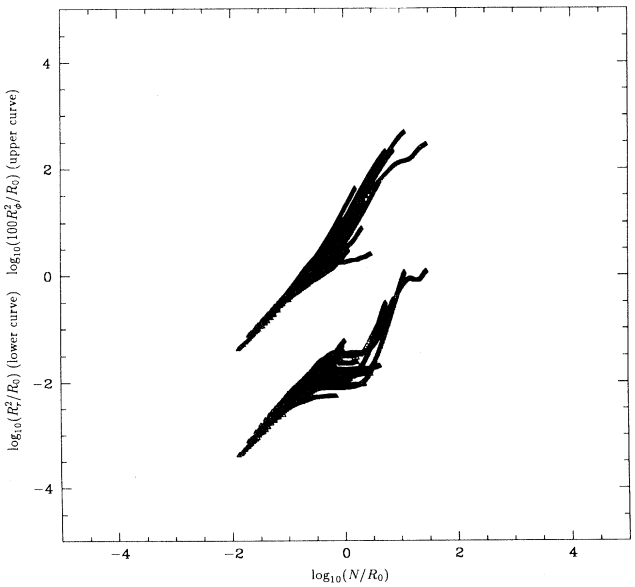

FIG. 15. Radial (R_r) and azimuthal (R_ϕ) radii of gyration near a supercoincidence site. The polymers are binned according to R_0, the distance of their initial point from the center of rotation. We have rescaled the radii and N by R_0 and collapsed all the data. The lower curve is $\log_{10}[R_r^2(N)/R_0]$ and the upper curve is $\log_{10}[R_\phi^2(N)/R_0]+2$.

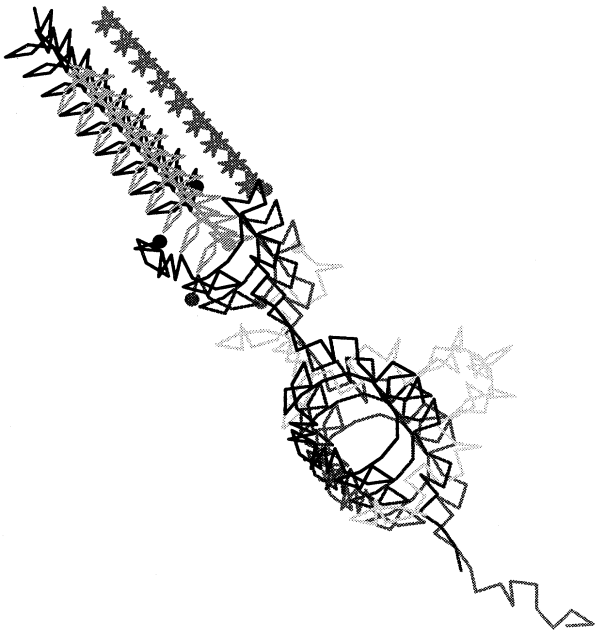

FIG. 16. Trajectories of seven nearest neighbors. The large dots represent the starting points of each polymer path.

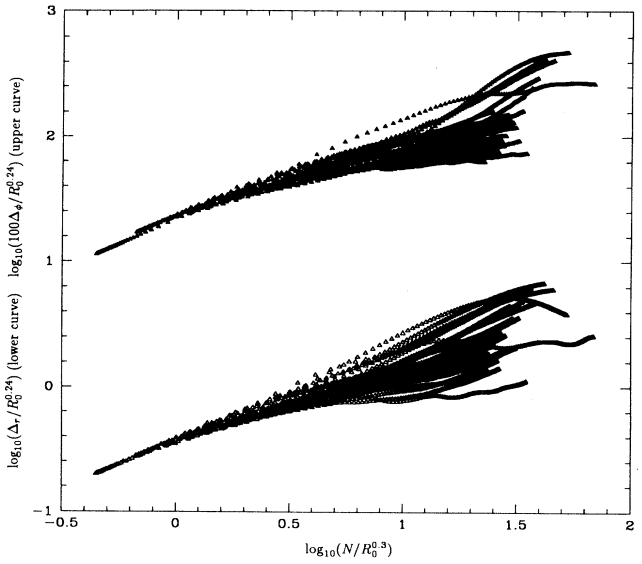

FIG. 17. Radial (Δ_r) and azimuthal (Δ_ϕ) root mean square separation of nearest neighbors near a supercoincidence site. The polymer groups are binned according to R_0, the distance of their initial point from the center of rotation. We plot the rescaled values of Δ versus $\log_{10}[N/R_0^{0.3}]$. The lower curve is $\log_{10}[\Delta_r(N)/R_0^{0.24}]$ and the upper curve is $\log_{10}[\Delta_\phi(N)/R_0^{0.24}]+2$.

$$\frac{\Delta_i(N,R_0)}{R_0}=N^{\bar{x}_i}B_i\left[\frac{N^{\bar{y}_i}}{R_0}\right]. \tag{6.7}$$

From our analysis we find that, again, for small N, $\Delta_i(N,R_0)$ does not depend on R_0. Thus $B_i(z)\to z$ as $z\to 0$ and, according to our data, $\bar{x}_i+\bar{y}_i=0.8$. Thus we will have the scaling form

$$\frac{\Delta_i(N,R_0)}{R_0^{0.8\nu_i}}=\tilde{b}_i\left[\frac{N}{R_0^{\nu_i}}\right], \tag{6.8}$$

where $\nu_i=1/\bar{y}_i$, $i=r,\phi$. We find the best collapse of data for $\nu_r=\nu_\phi=0.3$. The collapsed data are shown in Fig. 17. The separation between neighbors for small N is not quite ballistic. Presumably this is due to the fact that the polymers stay with their partners for some time before splitting apart as seen in the four rightmost paths in Fig. 16.

ACKNOWLEDGMENTS

It is a pleasure to acknowledge stimulating conversations with P. C. Hohenberg, T. C. Lubensky, J. F. Marko, R. B. Meyer, F. Spaepen, P. L. Taylor, E. L. Thomas, J. Toner, and G. Yan. R. D. K. acknowledges the hospitality of IBM Research Division, as well as support by National Science Foundation Grant No. PHY92-45317. D. R. N. acknowledges the hospitality of Brandeis University, AT&T Bell Laboratories, and Exxon Research and Engineering, as well as support from the Guggenheim Foundation and the National Science Foundation, through Grant No. DMR-9417047, and in part through the Harvard Materials Research Science and Engineering Center via Grant No. DMR-9400396.

APPENDIX: IRRATIONALITY OF LOCK-IN ANGLES

The special lock-in angles that we have found for the triangular lattice are all irrational fractions of 2π. We will prove a more general theorem in this appendix that applies to any rotation which leads to a coincidence lattice with a finite lattice constant. An alternate, algebraic proof appears in [18].

Consider two lattices with the second one rotated with respect to the first by an angle ϕ around a lattice point in common (so that if $\phi=0$ the lattices coincide). At certain "magic angles" ϕ_n there will form a lattice of points which are on both lattices. This is the coincidence lattice. Take the magic angle in question to be ϕ^*. If the angle is not an angle of symmetry of the lattice (e.g., $2\pi n/6$ for a triangular lattice) then the spacing of the coincidence lattice will be larger than the spacing on the original lattice by a factor of ζ. Now consider adding a third lattice, rotated again by ϕ with respect to the second lattice (i.e., rotated by 2ϕ from the first lattice and by ϕ from the second lattice). The first two lattices create a coincidence lattice and the second two lattices create a coincidence lattice. However, the last two lattices may be obtained by rotating the first two lattices by ϕ^*. Thus the coincidence lattice of the last two will be rotated by ϕ^* with respect to the coincidence lattice of the first two. Therefore the coincidence lattice of all three lattices will be the coincidence lattice of the two coincidence lattices and so the spacing of the supercoincidence lattice will be a factor of ζ^2 larger than the spacing of the original lattice.

This argument can now be extended to the coincidence lattice of n lattices. The first $(n-1)$ lattices form a coincidence lattice, as do the last $(n-1)$ lattices. These two coincidence lattices are rotated by ϕ^* from each other since the last $(n-1)$ lattices can be obtained by rotating each of the first $(n-1)$ lattices by ϕ^*. Thus the coincidence lattice of n lattices is the coincidence lattice of two $(n-1)$ coincidence lattices. This means that every time we add another rotated lattice, the coincidence lattice spacing grows by a factor of ζ and so the coincidence lattice of $(n+1)$ lattices is a factor of ζ^n larger than the original lattice spacing.

If the angle ϕ^* were a rational fraction of 2π, $\phi^*=2\pi p/q$, then after no more than q iterations the lattices would start to repeat. Thus upon adding the next lattice, the supercoincidence lattice would remain the same, and thus the lattice spacing would not grow. This implies that $\zeta^{q-1}=1$ and so the angle ϕ^* must be an angle of symmetry of the lattice. This proves that the lock-in angles are not rational fractions of 2π.

[1] B. Alberts *et al.*, *Molecular Biology of the Cell* (Garland, New York, 1989).
[2] F. Livolant, Physica A **176**, 117 (1981).
[3] Z. Reich, E. J. Wachtel, and A. Minsky, Science **264**, 1460 (1994).
[4] F. Livolant, Eur. J. Cell Biol. **33**, 300 (1984); Y. Bouligand, M. O. Soyer, and S. Puiseux-Dao, Chromosoma **24**, 251 (1968); R. L. Rill, F. Livolant, H. C. Aldrich, and M. W. Davidson, *ibid.* **98**, 280 (1989).
[5] J. P. Gourret, Biol. Cell. **32**, 299 (1978).
[6] V. Luzatti and A. Nicolaieff, J. Mol. Biol. **1**, 127 (1959); **7**, 142 (1963); M. Feughelman, R. Langridge, W. E. Seeds, A. R. Stokes, H. R. Wilson, M. H. F. Wilkins, R. K. Barclay, and L. D. Hamilton, Nature (London) **175**, 834 (1955).
[7] J. Lapault, J. Dubochet, W. Baschong, and E. Kellenberger, Eur. Mol. Biol. Organ. J. **6**, 1507 (1987).
[8] F. Livolant, A. M. Levelut, J. Doucet, and J. P. Benoit, Nature (London) **339**, 724 (1989).
[9] R. L. Rill, T. E. Strzelecka, D. H. Van Winkle, and M. W. Davidson, Physica A **176**, 87 (1991).
[10] F. Livolant and Y. Bouligand, J. Phys. (Paris) **47**, 1813 (1986); F. Livolant, J. Mol. Biol. **218**, 165 (1991).
[11] D. Van Winkle, M. Davidson, and R. L. Rill, J. Chem. Phys. **97**, 5641 (1992); K. Merchant, Ph.D. thesis, Florida State University, 1994.
[12] A. Le Forestier and F. Livolant, Biophys. J. **65**, 56 (1994).
[13] R. B. Meyer, F. Lonberg, V. Tarututa, S. Fraden, S. D. Lee, and A. J. Hurd, Disc. Faraday Chem. Soc. **79**, 125 (1985).
[14] H. Block, *Poly(γ-Benzyl-L-Glutamate) and other Glutamate Acid Containing Polymers* (Gordon and Breach, London, 1983).
[15] X. Ao, X. Wen, and R. B. Meyer, Physica A **176**, 63 (1991).
[16] S. R. Renn and T. C. Lubensky, Phys. Rev. A **38**, 2132 (1988); **51**, 4392 (1990).
[17] R. D. Kamien and D. R. Nelson, Phys. Rev. Lett. **74**, 2499 (1995).
[18] D. R. Nelson and R. D. Kamien, in *Proceedings of the Wiener 1994 Centennial Symposium,* edited by D. Jerison, I. M. Singer, and D. W. Stroock (American Mathematical Society, Providence, in press).
[19] S. Langer and J. Sethna, Phys. Rev. A **34**, 5035 (1986).
[20] G. A. Hinshaw, Jr., R. G. Petschek, and R. A. Pelcovits, Phys. Rev. Lett. **60**, 1864 (1988).
[21] J. V. Selinger and J. M. Schnur, Phys. Rev. Lett. **71**, 4091 (1993); J. V. Selinger, Z.-G. Wang, R. F. Bruinsma, and C. M. Knobler, Phys. Rev. Lett. **70**, 1139 (1993).
[22] See, for example, [35] and B. I. Halperin (unpublished).
[23] S. Meiboom, J. P. Sethna, P. W. Anderson, and W. F. Brinkman, Phys. Rev. Lett. **46**, 1216 (1981); D. C. Wright and N. D. Mermin, Rev. Mod. Phys. **61**, 385 (1989).
[24] P. G. de Gennes and J. Prost, *The Physics of Liquid Crystals,* 2nd ed. (Oxford University Press, New York, 1993), Chap. VII.
[25] L. Balents, R. D. Kamien, P. Le Doussal, and E. Zaslow, J. Phys. (France) I **2**, 263 (1992).
[26] R. B. Meyer, in *Polymer Liquid Crystals,* edited by A. Ciferri, W. R. Kringbaum, and R. B. Meyer (Academic, New York, 1982), Chap. 6.
[27] P. Le Doussal and D. R. Nelson, Europhys. Lett. **15**, 161 (1991); R. D. Kamien, P. Le Doussal, and D. R. Nelson, Phys. Rev. A **45**, 8727 (1992); Phys. Rev. E **48**, 4116 (1993).
[28] J. Toner, Phys. Rev. Lett. **68**, 1331 (1992).
[29] R. D. Kamien and J. Toner, Phys. Rev. Lett. **74**, 3181 (1995).
[30] J. Toner, Phys. Rev. A **27**, 1157 (1983).
[31] M. C. Marchetti and D. R. Nelson, Phys. Rev. B **41**, 1910 (1990).
[32] R. D. Kamien, Institute for Advanced Study Report No. IASSNS-HEP-95/44, 1995 (unpublished) (cond-mat/9507023).
[33] We thank J. Toner for discussions on this point.
[34] C. Gianessi, Phys. Rev. A **28**, 350 (1983); **34**, 705 (1986).
[35] D. R. Nelson and J. Toner, Phys. Rev. B **24**, 363 (1981).
[36] P. G. de Gennes, Solid State Commun. **14**, 997 (1973).
[37] A. M. Kosevich, Usp. Fiz. Nauk **84**, 579 (1964) [Sov. Phys. Usp. **7**, 837 (1965)].
[38] V. G. Taratura and R. B. Meyer, Liq. Cryst. **2**, 373 (1987).
[39] J. V. Selinger and R. F. Bruinsma, Phys. Rev. A **43**, 2910 (1991).
[40] V. L. Indenbom and A. N. Orlov, Usp. Fiz. Nauk **76**, 557 (1962) [Sov. Phys. Usp. **5**, 272 (1962)].
[41] R. Podgornik and V. A. Parsegian, Marcomolecules **23**, 2265 (1990).
[42] D. R. Nelson, in *Observation, Prediction and Simulation of Phase Transitions in Complex Fluids,* edited by M. Baus, L. F. Rull, and J.-P. Ryckaert (Kluwer, Dordrecht, 1995).
[43] J. Goodby, M. A. Waugh, S. M. Stein, R. Pindak, and J. S. Patel, Nature (London) **337**, 449 (1988); J. Am. Chem. Soc. **111**, 8119 (1989); G. Strajer, R. Pindak, M. A. Waugh, J. W. Goodby, and J. S. Patel, Phys. Rev. Lett. **64**, 13 (1990); K. J. Ihn, J. A. N. Zasadzinski, R. Pindak, A. J. Slanet, and J. Goodby, Science **258**, 275 (1992).
[44] M. Kléman, J. Phys. (Paris) **46**, 1193 (1985).
[45] T. C. Lubensky, T. Tokihiro, and S. R. Renn, Phys. Rev. Lett. **67**, 89 (1991).
[46] W. A. Bollman, *Crystal Defects and Crystalline Interfaces* (Springer-Verlag, Berlin, 1970); J. P. Hirth and J. Lothe, *Theory of Dislocations,* 2nd ed. (Wiley, New York, 1982).
[47] R. W. Balluffi, Y. Komem, and T. Schober, Surf. Sci. **31**, 68 (1992).
[48] E. M. Terentjev, Europhys. Lett. **23**, 27 (1993).

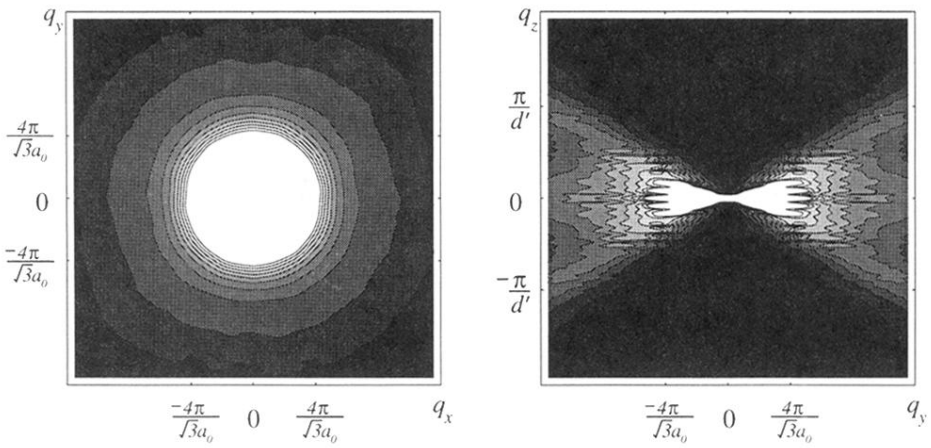

FIG. 14. Numerically calculated average Fourier transform of the monomer density of a single polymer in the (a) q_x-q_y and (b) q_y-q_z planes. We expect that a dilute concentration of deuterated polymers would produce neutron scattering profiles similar to these. The plots were made from the same data set as in Fig. 7.